The Pennsylvania State University

The Graduate School

College of Engineering

EXPERIMENTAL STUDY OF LOW-FIELD TRANSPORT IN HIGHLY CONFINED ARSENIDE-ANTIMONIDE QUANTUM WELL HETEROSTRUCTURES

A Thesis in
Electrical Engineering
by
Ashish Agrawal

© 2011 Ashish Agrawal

Submitted in Partial Fulfillment
of the Requirements
for the Degree of

Master of Science

August 2011

The thesis of Ashish Agrawal was reviewed and approved* by the following:

Suman Datta
Professor of Electrical Engineering
Thesis Advisor

Srinivas Tadigadapa
Professor of Electrical Engineering

Kultegin Aydin
Professor and Interim Department Head of Electrical Engineering

*Signatures are on file in the Graduate School.

Abstract

As Si approaches end of the roadmap, finding a new transistor technology that allows the extension of Moore's law has become a problem of great technical challenge and significance. Among the various candidates, III-V based MOSFETs are recognized as a very promising substitute. Specifically, low effective mass materials with high electron velocities, such as InAs and InSb are of great interest.

Mixed anion $\mathrm{InAs}_y\mathrm{Sb}_{1-y}$ quantum wells (QW) with high electron mobility are candidates for direct integration with high hole mobility $\mathrm{In}_x\mathrm{Ga}_{1-x}\mathrm{Sb}$ for ultra low power complementary applications. In order to understand the intrinsic performance of these high mobility materials, it is imperative to comprehend the factors that limit the mobility and how it changes as we scale the device for better short channel effects.

In this work, a comprehensive model based on the Momentum Relaxation Time approximation is formulated to determine the mechanisms limiting the mobility in the fabricated As-Sb quantum wells. The effect of conduction band nonparabolicity in the narrow bandgap InAsSb quantum well in transport and confinement direction of the E-k has been studied and incorporated in the transport model. All major scattering mechanisms, including acoustic phonons, polar optical phonons, alloy disorder, remote ionized impurities, interface roughness and interface charge scattering have been taken into account. The low-field electron transport properties of the 2DEG in the AlInSb/InAsSb quantum wells is studied as a function of temperature. Our model simultaneously explains the low-field electron transport in wide and scaled As-Sb devices. Finally, based on the calibrated model, we predict the low field performance for ultra scaled HEMT device for sub-10nm technology nodes.

Table of Contents

List of Figures vi

List of Tables x

Acknowledgments xi

Chapter 1

Introduction 1

1.1 Introduction to III-V CMOS 1

1.2 High Electron Mobility Transistors 3

1.3 The 6.1A Semiconductor Family 5

1.4 Thesis Outline 9

Chapter 2

Electron Transport in Confined System 11

2.1 Introduction 11

2.2 Density of States 11

2.2.1 Density of States Calculation 12

2.2.2 Density of States for Quantized Systems 14

2.3 Nonparabolicity of Conduction Band 16

2.4 Boltzmann Transport 20

2.4.1 Relaxation Time Approximation 22

2.5 Physical Models for Low-Field Electron Mobility in Quantum Wells . . 25

2.5.1 Acoustic Phonon Scattering 25

2.5.2 Polar Optical Phonon Scattering 27

2.5.3 Alloy Disorder Scattering 29

2.5.4 Remote Ionized Impurity Scattering 30

2.5.5 Interface Charge Scattering 31

2.5.6 Interface Roughness Scattering 31

Chapter 3

Transport in Mixed Anion As-Sb Quantum Well Heterostructures 34

3.1 Introduction 34

3.2 Scaling of HEMT 35

3.3 As-Sb Heterostructure Band Diagram 37

3.4 Hall Effect Measurement 39

3.5 Hall Sheet Charge Density 41

3.6 Low Field Mobility in Scaled As-Sb QW 43

3.7 Quantitative Mobility Spectrum Analysis 46

3.8 Effective Mass 47

Chapter 4

Conclusions 52

Bibliography 58

List of Figures

1.1 Electron mobility versus sheet electron density in n-channel FETs [2] . 2

1.2 A typical HEMT structure illustrating important structural and material aspects of the design 4

1.3 Energy gap versus lattice constant, showing the evolution of transistors to larger lattice constant and smaller bandgaps for high-frequency and low-power operation [8] 5

1.4 Band alignments for selected binary and alloy semiconductors at 0K [8] 7

1.5 Electron mobility versus sheet carrier concentration overlayed on a contour map of ballistic mean free path [15] 8

2.1 Calculation of the number of available energy states to accommodate electrons with wave number less than k [18] 13

2.2 Density of states versus energy for 3D semiconductor (blue cuve), 10nm quantum well (red curve), 10nm by 10nm quantum wire (green curve) and 10nmx10nmx10nm quantum dot [18] 16

2.3 (a) Schematic showing quantized energy levels in the quantum well due to structural quantization assuming parabolic E-k in confinement direction, (b) Schematic depicting decrease in subband energy levels due to band nonparabolicity in confinement direction. 18
2.4 Schematic comparing parabolic and nonparabolic dispersion in transport direction. Nonparabolicity increases the effective mass in transport direction. 19
2.5 A reference cell in two-dimensional position-momentum space illustrating the in-scattering and out-scattering processes affecting the distribution function 20
2.6 Longitudinal acoustic phonons are the crystal vibrations where atoms vibrate along the same direction 26
2.7 Longitudinal polar optical phonons are the crystal vibrations where the atoms vibrate along opposite direction 27
2.8 Figure showing interface roughness at barrier-QW interface resulting in electron scattering. 32

3.1 Subthreshold swing and DIBL vs. gate length for different QW thickness showing enhanced short channel effects with channel scaling [36] . 35
3.2 Threshold voltage shift as a function of QW width due to increased quantum confinement [37] 36
3.3 Simulated transport and confinement effective mass as a function of QW thickness calculated from tight binding calculations. Effective mass increases due to higher confinement and strong effect of nonparabolicity [37]. 37

3.4 Electron Hall mobility as a function of QW and barrier thickness [38]. . 38

3.5 Schematic of the $InAs_{0.8}Sb_{0.2}$ MOS-QWFET on GaAs substrate (a) with 12nm quantum well thickness and 9nm barrier layer, (b) with scaled 7.5nm quantum well thickness and 5nm barrier thickness. 39

3.6 Band diagram of $InAs_{0.8}Sb_{0.2}$ quantum well heterostructure with 12nm and 7.5nm quantum well thickness and 1nm GaSb interfacial layer from Schrodinger-Poisson simulation indicating strong electron confinement . 40

3.7 (a)Schematic and (b) Die shot of the hall structure fabricated on the wide and scaled quantum well heterostructures for performing hall measurements from temperature ranging from 4K to 300K 41

3.8 Experimental and modeled sheet charge density versus temperature in $InAs_{0.8}Sb_{0.2}$ quantum well channel for 12nm and 7.5nm quantum well thickness. The contribution from ground and first subband is indicated. . 42

3.9 Experimental and modeled electron mobility vs. temperature in InAsSb quantum well channel of 12nm and 7.5nm thickness, depicting dominant scattering mechanisms at low and room temperature. 44

3.10 Pareto plot showing % contribution of different scattering mechanisms to total mobility at 300K for thick and scaled QW. Interface charge scattering dominates for $T_{QW} = 12nm$ and interface roughness scattering dominates for $T_{QW} = 7.5nm$. 45

3.11 Quantitative Mobility Spectrum Analysis for thick and scaled InAsSb Quantum Well heterostructure for 77K, 200K and 300K and magnetic field ranging from 0T to 9T showing one electron peak corresponding to 2DEG in the QW. This indicates absence of parasitic parallel conduction in the semiconductor layers. 48
3.12 (a) Measured sheet resistance $\mathrm{R_{XX}}$ and (b) Hall resistance $\mathrm{R_{XY}}$ of the InAsSb QW heterostructure from 0-9 T. Insets in the figures show the configurations employed to measure $\mathrm{R_{XX}}$ and $\mathrm{R_{XY}}$ 49
3.13 Plot of $\ln(\Delta\rho_{XX}/\rho_0)$ versus $\ln(\chi/\sinh\chi)$ for (a) B=2.54 T and (b) B=3.01 T to extract effective mass. Correct value of effective mass gives a slope of 1 for the graph 50
3.14 Transport and confinement effective mass as a function of quantum well width in InAsSb quantum wells. The effect of nonparabolicity is more prominent in the confinement direction resulting in large increase in eff. mass for $\mathrm{T_{QW}} = 7.5\mathrm{nm}$. For reference, effective mass for InAs HEMT [37] has been shown for ultra scaled QW thickness. 51
4.1 Electron hall mobility vs. temperature for InAs/AlSb QW for different channel directions showing enhanced anisotropy in [1-10] direction [45]. 55
4.2 Schematic of a future As-Sb QW MOSFET structure. 56
4.3 (a) Calculated electron mobility and scattering mechanisms as a function of temperature for $\mathrm{T_{QW}} = 3\mathrm{nm}$, (b) calculated electron mobility as a function of temperature with reduced mean height of roughness and increased correlation length, showing improved performance. 57

List of Tables

1.1 Key parameters to important compound semiconductors belonging to the 6.1A family [7] 6

2.1 Nonparabolicity factors for various important materials [21] 18

3.1 Values of different parameters used for scattering rate calculation using Relaxation time approximation 44

Acknowledgments

I would like to thank, first and foremost, my adviser, Professor Suman Datta for his encouragement, guidance and continuous support throughout my research. He incessantly provided me with invaluable knowledge and great intuition during this research. Always teaching to aim for high standard of research, he imbibed in me, the much needed spirit of persistence and patience. I would also like to thank Professor Srinivas Tadigadappa for kindly agreeing to serve on my Master's committee. Special thanks to all the group members of Nanoelectronic Devices and Circuits Laboratory (NDCL) - Dheeraj, Lu, Feng, S. Vinay, R. Bijesh, Euichul, Salil. Thanks to Ashkar for providing me with fabricated devices and for valuable technical discussions.

This work would not have been possible without the assistance of Rajiv Misra and Professor Peter E. Schiffer from the Department of Physics at Penn State. I express my indebtedness to Rajiv for the Hall measurements and valuable discussions.

Lastly, nothing would have been possible without the inspiration, motivation and support of my family. To my parents and brother, thank you. Thank you for believing in me. Your love and encouragement was instrumental in my work and I dedicate this work to you.

Chapter 1

Introduction

1.1 Introduction to III-V CMOS

After almost 50 years of research, it is finally clear that there are technologies to make better-than-silicon MOSFET. Although the efforts were not sustained during this long time period with ups and downs, this area is now very active with yet growing interest of researches and engineers in electronic industry and academia. The number of papers published recently on III-V MOSFETs are way higher than at any given time in the past.

The bright hope comes from the much better electron transport properties of III-V materials with respect to Si which results from higher electron velocity. This directly contributes to high ON-state current and transconductance [1]. Therefore, to obtain higher electron velocity in future scaled down devices, III-V FETs have been getting more emphasis nowadays. Mobility is a good exponent of the excellent transport characteristics of III-Vs since electron velocity is mostly correlated to the mobility property. Figure 1.1 shows electron mobility as a function of sheet carrier density in various III-V quantum well heterostructures. It is apparent that most of the III-V FETs have about a hundred times larger electron mobility than conventional Si MOSFET.

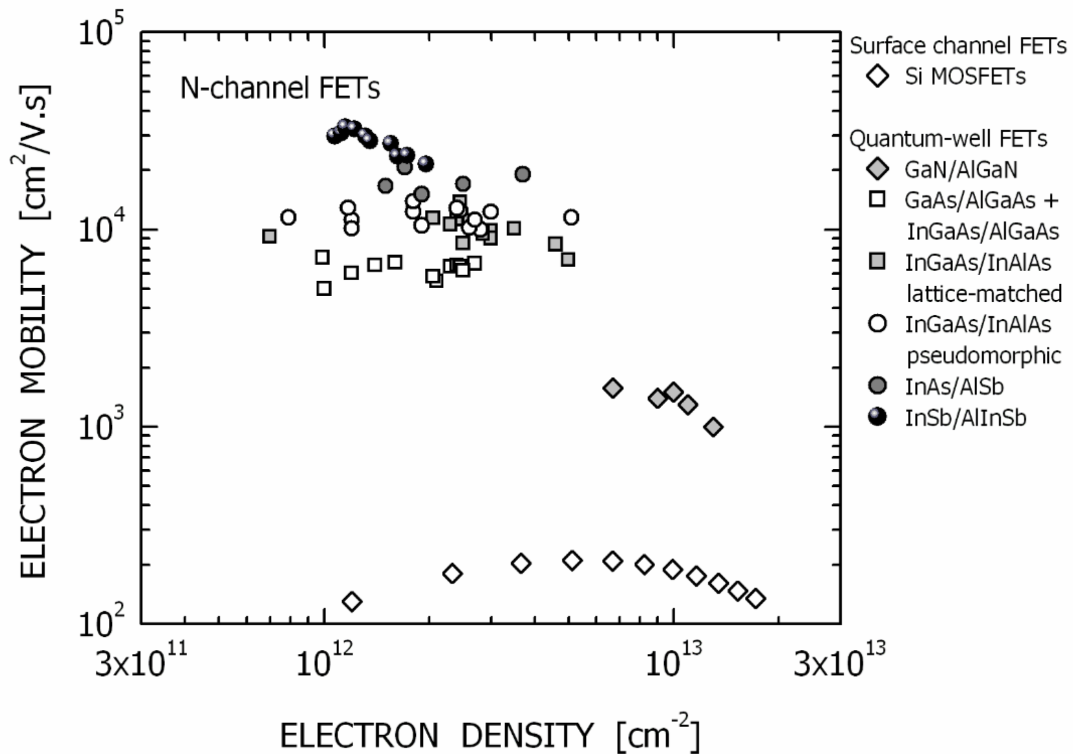

Figure 1.1: Electron mobility versus sheet electron density in n-channel FETs [2]

The high electron mobility originates from the low effective mass of the Γ valley in these materials. However, the Γ band is symmetric, meaning that the DOS and quantization effective masses are also small, which is undesirable. The low DOS mass will result in low charge density, and low quantization mass will result in high quantization leading to enhanced scattering. Furthermore, the low effective mass is only valid at the bottom of the conduction band. The non-parabolicity factor is typically large (and significant since the DOS effective mass is small), meaning that at higher energies the equivalent effective mass is quite large. This becomes important either at high carrier concentrations or when the carriers gain energy as they travel along the channel. The latter becomes important at the drain-side of the channel where the non-parabolicity limits the velocity overshoot.

Additionally, the separation between the Γ and the L and X band is usually not large. This combined with the low quantization effective mass of electrons in the Γ band, means that under strong quantum confinement of the satellite L and X bands will contribute to the electron transport. Not only do these bands have transport properties similar to the X and L bands in silicon and germanium, but also the additional interband scattering reduces the mobility further. Similarly, some of the high energy electrons near the drain are also transferred to the satellite valleys or have increased probability of having interband scattering.

From a manufacturing point of view, there are still lots of technical difficulties to overcome before III-V MOSFET can replace scaled Si MOSFET as a mainstream logic technology. One big challenge is to identify a suitable high-k gate dielectric material that makes low interface-state density (D_{IT}) near the conduction band edge [3] at the interface in semiconductor channel layer. It has another critical meaning because it can guarantee better gate-control with reduced vertical gate leakage which is essential for enhancement mode devices [4]. Integration of the III-V materials onto the Si substrate should be also achieved [5]. Since III-V substrates are difficult and expensive to grow in large area and are easily broken, integration technology into the Si substrate are necessary for being processed in current matured Si manufacturing infrastructure.

1.2 High Electron Mobility Transistors

High electron mobility transistors (HEMTs) are advantageous for low voltage, high frequency applications. They exhibit superior electron transport properties compared to other device structures. Advantages of a HEMT include high transconductance, high output resistance, and small source resistance. HEMTs are semiconductor devices with low noise and high Gain.BW characteristics. The usefulness of HEMT devices is appro-

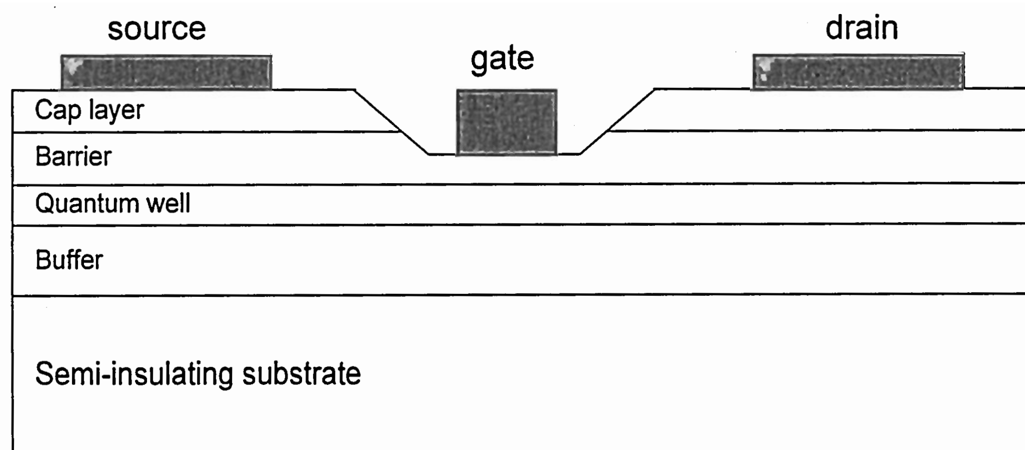

Figure 1.2: A typical HEMT structure illustrating important structural and material aspects of the design

priate for amplifier, receiver and detector applications. In silicon field effect transistors (FETs), a conducting channel is formed between two intentionally-doped regions. The channel region is also doped to generate charged carriers. In contrast, HEMTs utilize a unique feature, the heterojunction, which improves carrier confinement and electron transport. A HEMT structure is illustrated in Fig. 1.2. In a HEMT structure, the conduction carriers are physically separated from the donor impurities, which supply the electrons and reside in a lower energy state, confined by an energy barrier (the conduction band offset). During transistor operation, the charged carriers travel from the source to the drain by way of channel region. The conduction carriers become subject to impurity scattering in the channel. Because the conduction carriers are separated from the donor impurities in a HEMT structure, the effects of impurity scattering are reduced and high electron mobility values are attainable. The first high electron mobility transistors (HEMTs) were fabricated with GaAs channels and AlGaAs barriers [6].

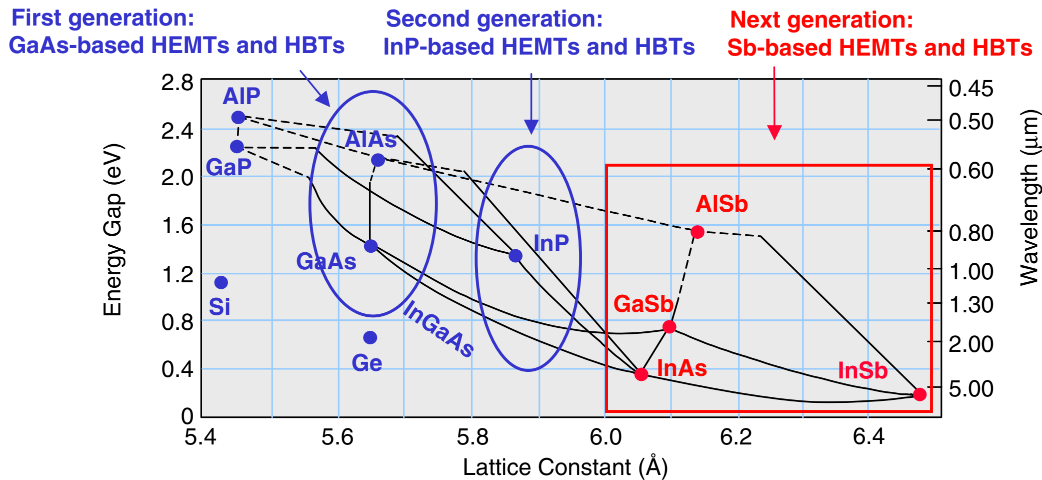

Figure 1.3: Energy gap versus lattice constant, showing the evolution of transistors to larger lattice constant and smaller bandgaps for high-frequency and low-power operation [8]

These devices are also known as modulation-doped field effect transistors (MODFET). In order to achieve higher electron mobility and velocity (translating to higher frequency operation), In was added to the channel. Typical structures have $In_{0.2}Ga_{0.8}As$ channels that are pseudomorphically strained to the GaAs lattice constant (PHEMTs). In order to improve performance further, additional In was added to the channel and the barrier material was changed to InAlAs; the larger lattice constants were accommodated by using InP substrates.

1.3 The 6.1A Semiconductor Family

The logical progression of this trend is to use pure InAs as the channel along with nearly lattice matched AlSb, AlGaSb or InAlSb for the confining layer as the arsenides are not suitable barriers. Advantages of this material system include the high electron mobility

Parameter	InAs	InSb	GaSb
Lattice constant [A]	6.059	6.479	6.095
Bandgap [eV]	0.354	0.17	0.726
Electron Effective mass	0.023	0.014	0.041
Conduction Band DOS [cm^{-3}]	8.7E16	4.2E16	2.1E17
Optical Phonon energy [meV]	30	25	29.7

Table 1.1: Key parameters to important compound semiconductors belonging to the 6.1A family [7]

(30,000 $\mathrm{cm}^2/\mathrm{Vs}$ at 300K) and velocity ($4\mathrm{x}10^7$ cm/s) of InAs [9] and a large conduction band offset between InAs and AlSb (1.35 eV), as shown in Fig. 1.3. Most of the recent advances in antimonide-based HEMTs have involved heterostructures grown by molecular beam epitaxy (MBE). Antimonide growth by MBE was first reported in the late 1970s [10]. The growth of antimonide and mixed antimonide/arsenic structures by MBE has presented some challenges compared to growth of arsenides [11]. Overall growth of antimonides is simpler than nitrides and does not present the safety issues associated with phosphides. Crucial advances for transistor applications were reported by Prof. Kroemer's group at the University of California at Santa Barbara, beginning in the late 1980s. They grew InAs/AlSb single quantum wells and showed that high mobilities could be achieved by controlling the interfaces [12, 13]. The interface bonds can be either InSb-like or AlAs-like as there is no common cation or anion for a heterojunction between InAs and AlSb. Work by Tuttle et. al. showed that the bottom interface must be InSb-like or AlAs-like as there is no common cation or anion for a heterojunction between InAs and AlSb. Bolognesi et. al. varied the thickness of the InAs quantum well and achieved high mobilities for 125-200 A [14]. AlSb and GaSb, in comparison to InAs, exhibit larger energy gaps and inferior transport properties. Selected properties for InAs, GaSb and AlSb are provided in Table 1.1.

The 6.1A semiconductor family has drawn a great deal of interest for the large con-

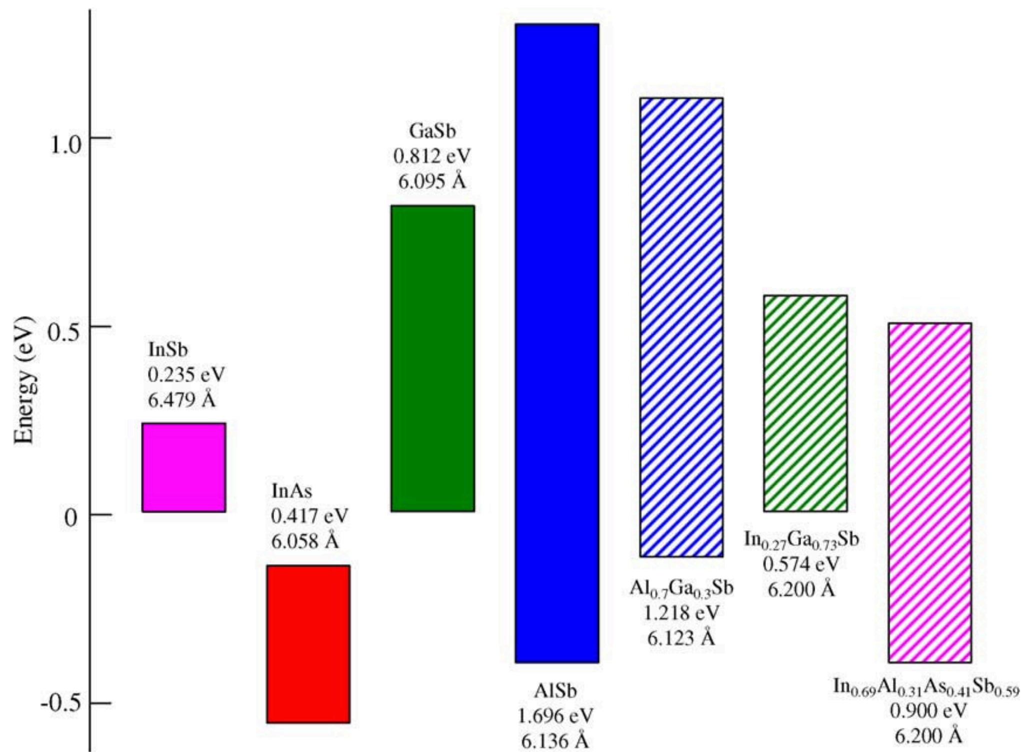

Figure 1.4: Band alignments for selected binary and alloy semiconductors at 0K [8]

duction band offsets between AlSb and InAs (1.35 eV) and small lattice mismatch (<1.2%). A large conduction band offers carrier confinement and allows high carrier densities and mobilities to be achieved. Because of band alignments and small lattice mismatch among these materials, various device structures can be explored with interesting quantum properties. For example, both type-I and type-II structures can be achieved with the 6.1A semiconductor family. By varying composition, the following can be produced: straddling type-I band alignments (AlSb/GaSb), type-II staggered band alignments (AlSb/InAs), and type-II broken band alignments (GaSb/InAs). The energy band alignments are presented in Figure 1.4. Unique to these material systems is the range of band alignments that can be accomplished without considerable differences in bulk lattice spacing at the interface, which is not the characteristic of most material

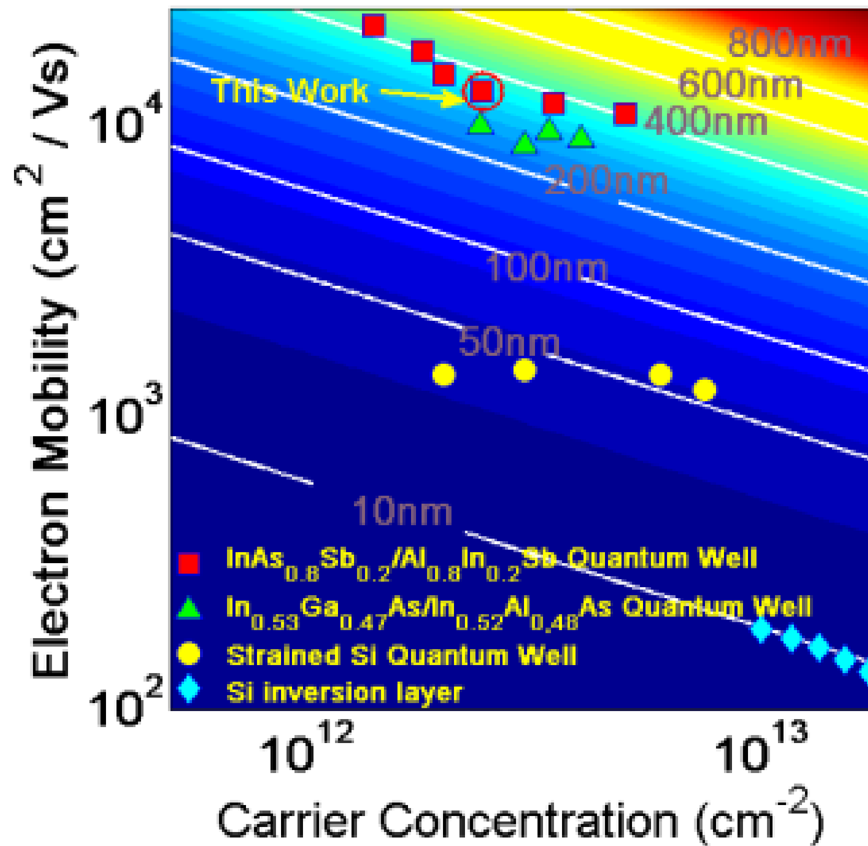

Figure 1.5: Electron mobility versus sheet carrier concentration overlayed on a contour map of ballistic mean free path [15]

systems. As a result, the crystalline quality of these structures can be retained without the effects of severe lattice deformation.

Moving to a 6.2A lattice constant structure for the HEMT has many additional benefits, including a type I band alignment between barrier and channel layers. Owing to the high peak velocity of electrons in narrow band gap semiconductor device channels, impact ionization becomes a significant problem as holes are generated in the channel. The addition of Sb raises the valence band offset for the InAs(Sb) relative to the AlSb resulting in a desirable type I band alignment. This band alignment acts to confine the holes to the channel limiting them from drifting to the gate as a leakage current or transferring to the AlSb barrier where they become trapped and act as an unwanted bias. For

digitally grown InAsSb quantum wells it has been shown that the band alignment goes to a type I when the Sb atom fraction is 15% [16]. Another potential advantage is that the electrons in the InAsSb channel have a smaller effective mass than electrons in the InAs channel leading to the possibility of higher peak carrier velocities. The transition to the 6.2 A structure also involves the replacement of AlSb with InAlSb. The addition of small amounts of In to the AlSb improves the oxidation resistance significantly [17], and as a result, the device processing has more flexibility and the final device is more reliable and stable. Fig. 1.5 shows the mobility vs sheet density of InAsSb quantum well heterostructures alongside other important III-V heterostructures.

1.4 Thesis Outline

In this thesis, we aim to develop a detailed understanding of the electron transport in the AlInSb/InAsSb heterostructure by experimentally and theoretically studying the low-field mobility of the device heterostructures with varying barrier thickness and channel thickness. We present the results of Hall mobility measurements performed on wide and scaled $\mathrm{InAs_{0.8}Sb_{0.2}}$ quantum well channel with $\mathrm{Al_{0.8}In_{0.2}Sb}$ barrier. Both the quantum well thickness and barrier thickness were scaled down and the effect on Hall mobility was measured and analyzed. Although the Hall mobility measurement does not exactly match the drift or effective channel mobility, evaluation of which is complicated due to high interface trap density at III-V/high-k interface, it allows for more reliable measurements of the intrinsic channel transport.

This thesis will be organized in the following way. Chapter 2 will start with the physics of electrons in a confined system. The physical properties of electrons in two, one and zero dimensional system will be reviewed. The nonparabolicity model for the computation of charge density is discussed next. Furthermore, we review the Boltz-

mann Transport equation (BTE) and the relaxation time approximation (RTA) formalism, which is then used to derive the scattering rate expression for the various scattering mechanisms considered to explain the experimental mobility data.

In chapter 3, the experimental InAsSb QW MOSHEMT devices studied in this work will be described. Two set of devices were fabricated, one with wide quantum well, another with scaled quantum well and barrier thickness. Next, we simulate the wide and scaled structure using a 1-D Schrodinger-Poisson Solver (Nextnano) simulation tool. The obtained band diagram shows type I band alignment between barrier and channel. Additionally, the eigenenergies, wavefunctions and the position of the fermi level is shown for the specified carrier density. Sheet charge density in the quantum well is modeled as a function of temperature and contributions from ground and first subbands is determined, which is then used in transport modeling. Low-field mobility is modeled for wide and scaled QW devices using relaxation time expressions for scattering mechanisms discussed in chapter 2, and important conclusions were made. Experimental study of effective mass using Shubnikov-de Haas method is performed on thick QW device and transport mass extracted. We present QMSA of the thick and scaled QW device, showing contribution of different carrier species in the heterostructure layers.

Finally, in chapter 4, we summarize all the key conclusions from the transport analysis work and provide suggestions for performance improvement. Additionally, we predict the mobility and scattering mechanisms based on our model for the ultimate scaled device with L_G=10nm.

Chapter 2

Electron Transport in Confined System

2.1 Introduction

In this chapter, we touch upon the physics for electron transport in a confined system. We review Schrodinger's equation, nonparabolicity model for charge in quantum wells, Boltzmann Transport equation and Momentum Relaxation Time approximation formalism. Subsequently, these shall be used to calculate the band structure and to model electron transport behavior in the InAsSb quantum well heterostructure.

2.2 Density of States

Density of states refers to the number of states that a carrier can occupy per unit volume per unit energy at a specific temperature. By multiplying the density of states with the probability that a state is occupied can give the number of electrons at each energy level per unit volume [18].

2.2.1 Density of States Calculation

The density of states (DOS) in a semiconductor crystal with periodic potential is estimated as the density per unit volume and energy of the number of solutions to the Schrodinger's equation [18]. Consider a cubic piece of semiconductor with a side L. Assume that this can be modeled as an infinite quantum well with potential in the well taken as zero. The electrons in the well are free to move with an effective mass of m*. Schrodinger's equation along the x direction is given by (2.1)

$$\frac{-\hbar^2}{2m^*}\frac{d^2\psi(x)}{dx^2} + V(x)\psi(x) = E\psi(x) \tag{2.1}$$

Boundary conditions are $\psi(x)$=0 at x=0 and x=L. The solutions to wave equation are of the form

$$\psi(x) = A\sin(k_x x) + B\cos(k_x x) \tag{2.2}$$

where A and B are constants. On applying the boundary conditions we get,

$$k_x = \frac{n\pi}{L}, \quad n = 1, 2, 3... \tag{2.3}$$

Similar analysis can be done for y and z direction. Each possible solution of the Schrodinger's equation then corresponds to a cube in the k-space with size $n\pi/L$ as shown in Fig. 2.1.

The total number of solutions to Schrodinger's equation can be found by dividing the total volume in the first quadrant of the sphere with radius 'k' by the volume corresponding to a single solution. This has to be multiplied by a factor of 2 to account for the two possible spins for a given rate. The total number of states in a volume of L^3 is

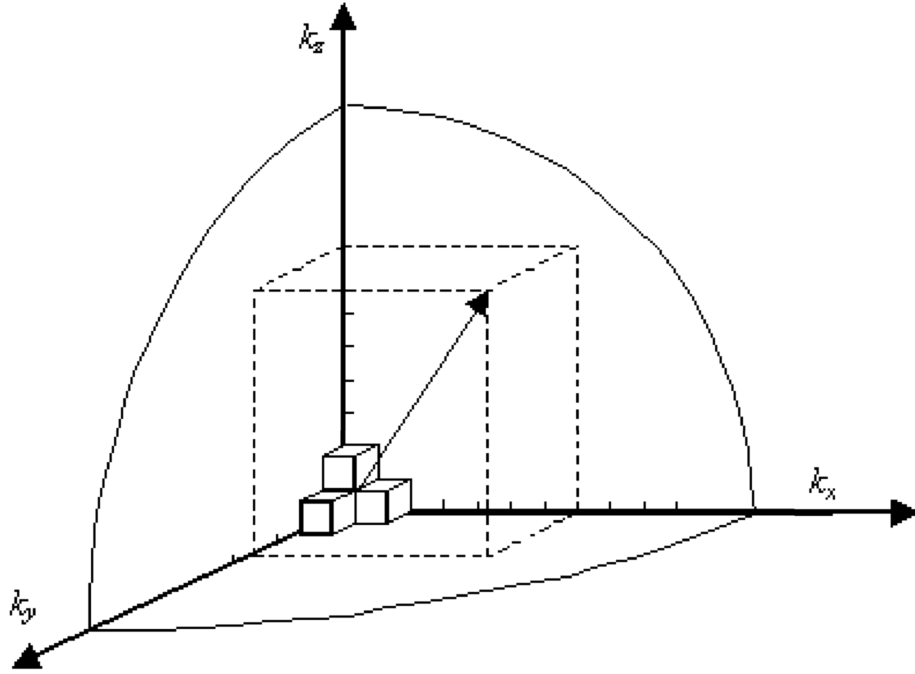

Figure 2.1: Calculation of the number of available energy states to accommodate electrons with wave number less than k [18]

given by (2.4)

$$N = \frac{4}{3}\pi k^3 \frac{1}{8}\left(\frac{L}{\pi}\right)^3 \cdot 2 \tag{2.4}$$

The density per unit energy is given by

$$\frac{dN}{dE} = \frac{dN}{dk}\frac{dk}{dE} = \left(\frac{L}{\pi}\right)^3 \pi k^2 \frac{dk}{dE} \tag{2.5}$$

For the parabolic E-k relationship,

$$E = \frac{\hbar^2 k^2}{2m^*} \rightarrow \frac{dk}{dE} = \frac{m^*}{\hbar^2 k} \,\text{where}\, k = \sqrt{\frac{2m^* E}{\hbar^2}} \tag{2.6}$$

Density of states, the number of states per unit volume per unit energy is given by

$$g(E) = \frac{1}{L^3}\frac{dN}{dE} = \frac{8\pi\sqrt{2}}{h^3} m^{*3/2}\sqrt{E}, \quad \text{for } E \geq 0 \tag{2.7}$$

The above expression is defined for E>0. For electrons in the conduction band, the minimum energy position is the bottom of the conduction band, E_c. The DOS for conduction band electrons can be expressed as given in (2.8,

$$g_c(E) = \frac{8\pi\sqrt{2}}{h^3} {m_c}^{*3/2}\sqrt{E - E_c}, \quad \text{for } E \geq E_c \tag{2.8}$$

where m_c is the effective mass that describes the curvature of the conduction band. Similar expression for DOS can be written for holes in the valence band as in (2.9).

$$g_v(E) = \frac{8\pi\sqrt{2}}{h^3} {m_v}^{*3/2}\sqrt{E_v - E}, \quad \text{for } E \leq E_v \tag{2.9}$$

where m_v is the effective mass which describes the curvature of the valence band.

2.2.2 Density of States for Quantized Systems

The above expression for DOS is valid for a bulk semiconductor where the carriers are free to move in all the three spatial dimensions. In other words, carriers in a bulk semiconductor have three degrees of freedom and there will be a continuum of energy levels in the conduction and valence bands. If one of the physical dimensions of the material is reduced so that the motion of carriers in that direction is restricted, then the continuum of energy levels that normally exists in the conduction band or valence band of solids is transformed into a set of discrete energy states or quanta [18]. Number of

states between k and $k + dk$ in 1, 2 and 3 dimensions is given by,

$$\frac{dN_{3D}}{dk} = 2\left(\frac{L}{2\pi}\right)^3 4\pi k^2 \tag{2.10}$$

$$\frac{dN_{2D}}{dk} = 2\left(\frac{L}{2\pi}\right)^2 2\pi k \tag{2.11}$$

$$\frac{dN_{1D}}{dk} = 2\left(\frac{L}{2\pi}\right) \tag{2.12}$$

For a bulk semiconductor, the expression for DOS is same as in (2.8). For a quantum well where particles are confined to a plane, DOS can be written as

$$g_{c,2D}(E) = \frac{4\pi}{h^2}m^*, \quad \text{for } E \geq E_{min} \tag{2.13}$$

This expression is only considering the first energy level. This has to be summed along all the quantized energy levels to get the final density of states, which will be a staircase function given by

$$g_{c,2D}(E) = \frac{4\pi}{h^2}m^* \sum H(E - E_n) \tag{2.14}$$

where $H(E - E_n)$ is the Heaviside step function which will be 0 for $E < E_n$ and 1 for $E > E_n$ and n is the quantum number along the quantized direction.

For the case of a quantum wire in which particles are confined along a line, 2D confinement gives rise to two quantum numbers n_1 and n_2.

$$g_{c.1D}(E) = 2\sqrt{\frac{2\pi}{h^2}m^*} \sum_i \frac{1}{\sqrt{E - E_{n1n2}}} H(E - E_{n1n2}) \tag{2.15}$$

For a 0-D structure or a quantum dot, the k values will be quantized in x, y and z

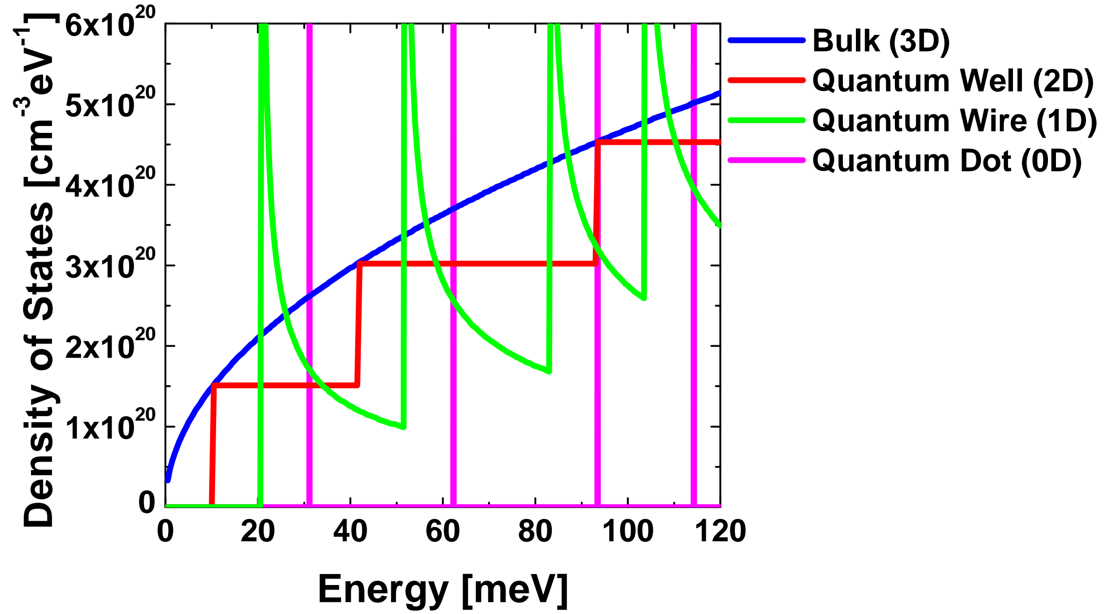

Figure 2.2: Density of states versus energy for 3D semiconductor (blue cuve), 10nm quantum well (red curve), 10nm by 10nm quantum wire (green curve) and 10nmx10nmx10nm quantum dot [18]

directions. Available energies will be discrete and DOS can be represented as delta functions at those allowed energies. The graphical representation of the DOS for 3D (bulk), 2D (quantum well), 1D (quantum wire) and 0D (quantum dot) is shown in Fig. 2.2

2.3 Nonparabolicity of Conduction Band

If the band structure is known, $E(k)$ can always be expanded in a Taylor series as

$$E(k) = E(0) + \left.\frac{\partial E(k)}{\partial k}\right|_{k=0} k + \left.\frac{\partial^2 E(k)}{\partial k^2}\right|_{k=0} k^2 + ... \tag{2.16}$$

When the band minimum occurs at k=0, the gradient of $E(k)$ is zero at k=0, so, we can approximate,

$$E(k) = E(0) + \frac{\hbar^2 k^2}{2m^*} \tag{2.17}$$

where

$$\frac{1}{m^*} = \frac{1}{\hbar^2}\frac{\partial^2 E(k)}{\partial k^2} \tag{2.18}$$

For high applied fields, carriers may be far above the minimum, and the higher order terms in the Taylor series expansion cannot be ignored. For the conduction band the nonparabolicity is often described by a relation known as the Kane's simplified model

$$E(1 + \alpha E) = \frac{\hbar^2 k^2}{2m^*_\Gamma} \tag{2.19}$$

where α is the conduction band nonparabolicity factor. m* is determined from Eq. (2.20)

$$m^*(E) = \hbar^2 k \left(\frac{\partial E(k)}{\partial k}\right)^{-1} \tag{2.20}$$

rather than Eq. (2.18) [19]. The traditional definition of the electron effective mass is not valid for nonparabolic semiconductors because an assumption of the constant, energy independent effective mass was made in the derivation of this relation.

Fig. 2.3a shows the position of the eigenenergies in the quantum well which are obtained by using parabolic approximation of the E-k in confinement direction. However, if the effect of nonparabolicity is substantial, as is the case with most of the narrow bandgap III-V semiconductors, the energy of the subbands will be lower than that predicted by the parabolic approximation as shown in Fig. 3.7b. In other words, the effect of quantization is reduced significantly because of band nonparabolicity in confinement. Even if the width of quantum well is reduced significantly, the effect of structural confinement on the energy of the subbands will be reduced than what would be expected

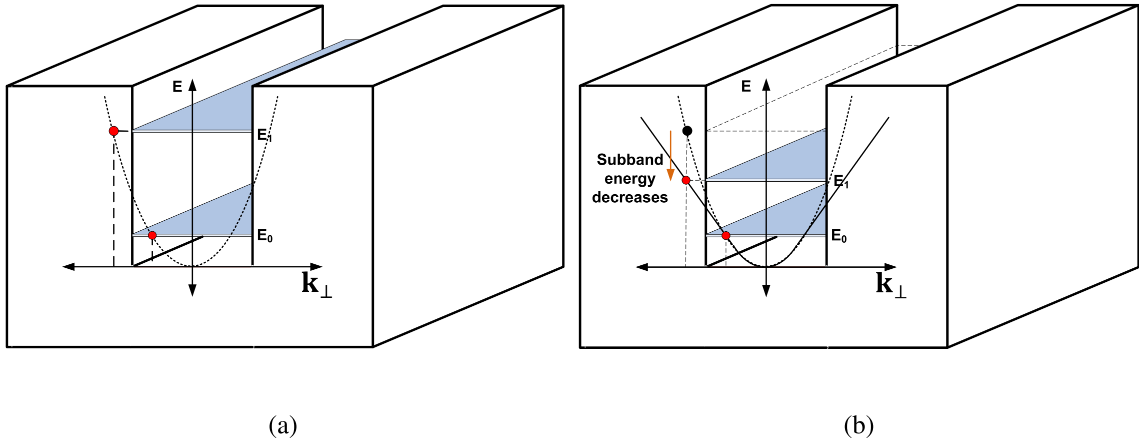

(a) (b)

Figure 2.3: (a) Schematic showing quantized energy levels in the quantum well due to structural quantization assuming parabolic E-k in confinement direction, (b) Schematic depicting decrease in subband energy levels due to band nonparabolicity in confinement direction.

Material	α [eV^{-1}]
Si	0.5
Ge	0.65
GaAs	0.64
GaSb	1.36
InP	0.67
InAs	2.73
InSb	5.72

Table 2.1: Nonparabolicity factors for various important materials [21]

from parabolic approximation. This has important repercussions on mobility as lower subband energy lead to higher intersubband scattering.

Fig. 2.4 shows the effect of nonparabolicity in transport direction. Lower curvature of E-k leads to increased electron transport mass for both the subbands, especially when the energy of carriers is high.

Table 2.1 shows the conduction band nonparabolicity factors of important compound semiconductors.

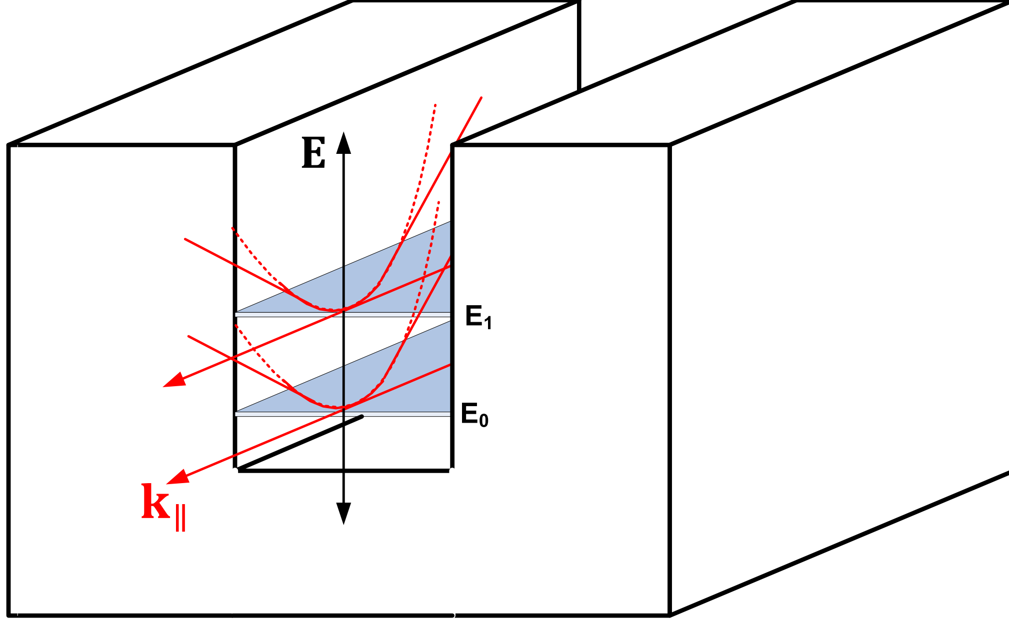

Figure 2.4: Schematic comparing parabolic and nonparabolic dispersion in transport direction. Nonparabolicity increases the effective mass in transport direction.

The density of states for a nonparabolic conduction band will deviate from the parabolic approximation. Carrier population of the *j*th subband can be described using the Fermi-Dirac statistics as shown in Eq. (2.21),

$$N_j(E_f, E_j) = \frac{m_\Gamma^*}{\pi\hbar^2}\int_{E_j}^{\infty}\frac{1+2\alpha E}{1+\exp[(E-E_f)/k_BT]}dE \tag{2.21}$$

where E_j and E_f are the position of the *j*th subband and fermi level with respect to the conduction band edge, m_Γ^* is the effective mass at the bottom of the conduction band. If more than one subband is occupied, the total carrier density is the sum of N_j over all subbands.

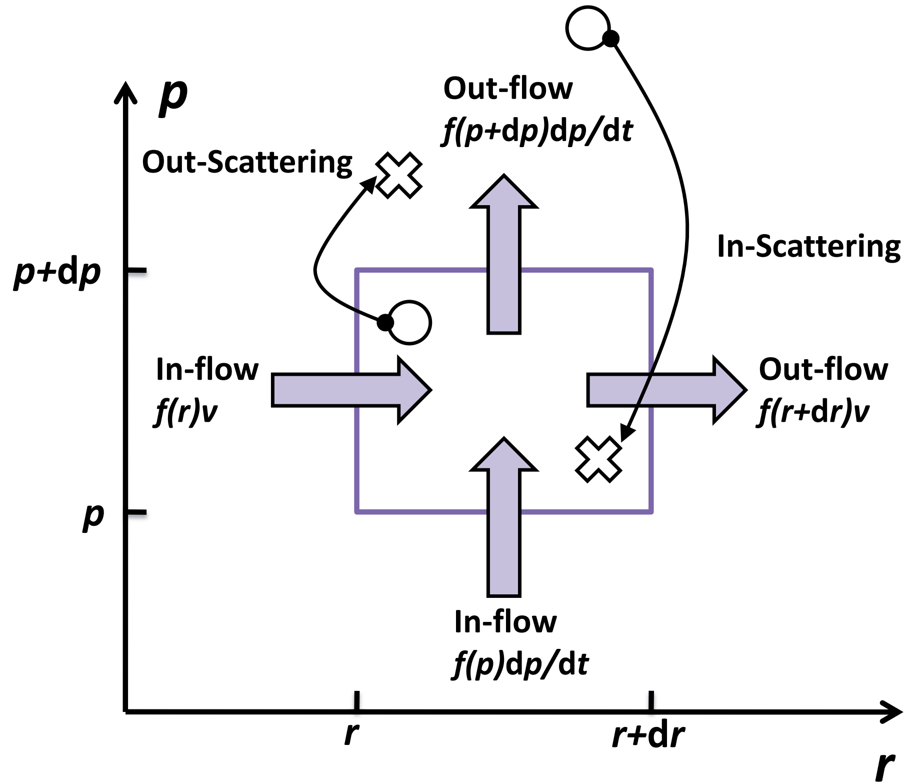

Figure 2.5: A reference cell in two-dimensional position-momentum space illustrating the in-scattering and out-scattering processes affecting the distribution function

2.4 Boltzmann Transport

In order to completely understand the operation of a device, the state of each carrier of the device should be known. For classical particles, we should know each carrier's position and momentum as a function of time. $f(\mathrm{r}, \mathrm{p}, t)$ is the probability of finding a carrier with crystal momentum p, at location r and at time t and has value between zero and one. To find $f(\mathrm{r}, \mathrm{p}, t)$ we solve the Boltzmann Transport Equation (BTE). The solution to BTE describes the average distribution of carriers in both position and momentum and can be used to obtain various quantities of interest such as the carrier, current and kinetic energy densities.

The BTE is just a bookkeeping equation for $f(\mathrm{r}, \mathrm{p}, t)$ which accounts for all possible

mechanisms by which f may change. Consider a region in two-dimensional position-momentum space as shown in Fig. 2.5. In a time $\delta t, f$ may increase within the region shown if the in-flow exceeds the out-flow in both position and momentum space, or if there is a net generation of carriers or if collisions send carriers from other cells to the one shown. Conservation of carriers requires that

$$\begin{aligned}(\delta f \delta r \delta p) &= [f(r) - f(r + \delta r)] v \delta t \delta p + [f(p) - f(p + \delta p)] F \delta t \delta r \\ &\quad + \left[s(r,p,t) + \partial f / \partial t \Big|_{coll} \right] \delta t \delta r \delta p \end{aligned} \tag{2.22}$$

After rearranging the terms and letting δt, δr and δp approach zero, we deduce

$$\frac{\partial f}{\partial t} = -v \frac{\partial f}{\partial r} - F \frac{\partial f}{\partial p} + \frac{\partial f}{\partial t}\Big|_{coll} + s(r,p,t) \tag{2.23}$$

which is the BTE for one space and one momentum dimension. Generalizing this result to a six-dimensional position-momentum space, we find

$$\frac{\partial f}{\partial t} + v \cdot \nabla_r f + F \cdot \nabla_p f = \frac{\partial f}{\partial t}\Big|_{coll} + s(r,p,t) \tag{2.24}$$

where

$$\nabla_r f = \frac{\partial f_x}{\partial x} \hat{x} + \frac{\partial f_y}{\partial y} \hat{y} + \frac{\partial f_z}{\partial z} \hat{z} \tag{2.25a}$$

$$\nabla_p f = \frac{\partial f_x}{\partial p_x} \hat{x} + \frac{\partial f_y}{\partial p_y} \hat{y} + \frac{\partial f_z}{\partial p_z} \hat{z} \tag{2.25b}$$

Equation 2.24 is the Boltzmann transport equation [21]; its solution provides the distribution function from which macroscopic quantities of interest are readily evaluated. $-(v \cdot \nabla_r f + F \cdot \nabla_p f)$ in the BTE represents net in-flows. The first term is an in-flow in position space and the second is an in-flow in momentum space. The ‘generation-

recombination' term in the BTE consists of two components. The first describes actual carrier generation recombination processes such as photogeneration or recombination through defects by the function $s(r, p, t)$. Collisions displace carriers from one momentum state to another and also produce sources and sinks in momentum space.

2.4.1 Relaxation Time Approximation

Scattering alters the distribution function by two processes - carriers at p' could be scattered to p thereby increasing f - in-scattering process ; carriers at p could scatter out decreasing f - out-scattering process. The net rate of increase of $f(r, p, t)$ due to collisions is a result of the competition between in-scattering and out-scattering and is given by

$$\left.\frac{\partial f}{\partial t}\right|_{coll} = \sum_{p'} f(p')[1 - f(p)]S(p', p) - \sum_{p'} f(p)[1 - f(p')]S(p, p') = \hat{C}f \tag{2.26}$$

where $\hat{C}$ is the collision operator. For the in-scattering process, *f(p')* gives the probability that a carrier is at *p'*, and $[1 - f(p)]$ is the probability that the state at p is empty. The transition rate S(p',p) is the probability per second that a carrier at p' will scatter to p. The sum is over p' - all of the possible state from or to which carriers may scatter. For non-degenerate semiconductors, $f(r, p, t) \ll 1$ and the $[1 - f(p)]$ terms can be set to one, so

$$\left.\frac{\partial f}{\partial t}\right|_{coll} = \sum_{p'} f(p')S(p', p) - \sum_{p'} f(p)S(p, p') \tag{2.27}$$

Most conventional device simulations are based on approximate models for transport which are derived from the Boltzmann equation, coupled to Poisson's equation for self-consistency. In the simplest approach, the relaxation time approximation is invoked, where the total distribution function is split into a symmetric term in terms of momentum

(which is generally large) and an asymmetric term (which is generally small).

$$f(r,p,t) = f_S(r,p,t) + f_A(r,p,t) \tag{2.28}$$

For non-degenerate semiconductors, the collision integral may be written as

$$\left.\frac{\partial f}{\partial t}\right|_{coll} = \left.\frac{\partial f_S}{\partial t}\right|_{coll} + \left.\frac{\partial f_A}{\partial t}\right|_{coll} \tag{2.29}$$

We consider two cases:

1. Equilibrium conditions:

$$f_S = f_0,\ f_A = 0 \rightarrow \left.\frac{\partial f}{\partial t}\right|_{coll} = \left.\frac{\partial f_S}{\partial t}\right|_{coll} \tag{2.30}$$

2. Non-equilibrium conditions when $f_A \neq 0$. In this case, we must consider two different situations

   - Low-field conditions, where f_S retains its equilibrium form with $T_C = T_L$ where T_C and T_L is the carrier and lattice temperature respectively. In this case $\partial f_S/\partial t|_{coll} = 0$.
   - High-field conditions when $T_C \neq T_L$ and does not retain its equilibrium form. In this case $\partial f_S/\partial t|_{coll} \neq 0$.

In all of these cases, a plausible form for the term $\partial f_A/\partial t|_{coll}$ is

$$\left.\frac{\partial f_A}{\partial t}\right|_{coll} = -\frac{f_A}{\tau_f} \tag{2.31}$$

where τ_f is a characteristic time that describes how the distribution function relaxes to its equilibrium form. With the above discussion, we can conclude that

- At low fields:

$$\left.\frac{\partial f}{\partial t}\right|_{coll} = \left.\frac{\partial f_A}{\partial t}\right|_{coll} = -\frac{f_A}{\tau_f} \tag{2.32}$$

- At high fields:

$$\left.\frac{\partial f}{\partial t}\right|_{coll} = \left.\frac{\partial f_S}{\partial t}\right|_{coll} + \left.\frac{\partial f_A}{\partial t}\right|_{coll} = \left.\frac{\partial f_S}{\partial t}\right|_{coll} - \frac{f_A}{\tau_f} \tag{2.33}$$

To have a more clear understanding of the relaxation time, we consider a semiconductor in which there are no spatial and momentum gradients. With the gradient terms zero, the BTE becomes

$$\frac{\partial f}{\partial t} = \left.\frac{\partial f_A}{\partial t}\right|_{coll} = -\frac{f_A}{\tau_f} = -\frac{f - f_0}{\tau_f} \tag{2.34}$$

$$\frac{\partial f}{\partial t} + \frac{f}{\tau_f} = \frac{f_0}{\tau_f} \tag{2.35}$$

The solution of this first-order differential equation is

$$f(t) = f_0 + [f(0) - f_0]e^{-t/\tau_f} \tag{2.36}$$

This result suggests that any perturbation in the system will decay exponentially with a characteristic time constant τ_f. It also suggests that the RTA is only good when $[f(0) - f_0]$ is not very large. Note that an important restriction for the relaxation time approximation to be valid is that τ_f is independent of the distribution function and the applied electric field.

2.5 Physical Models for Low-Field Electron Mobility in Quantum Wells

The transition probability is calculated with the help of quantum mechanics. The scattering rate for an electron scattered from an initial state *p* to a final state *p'* is given by the following relation according to quantum mechanics:

$$S(p, p') = \frac{2\pi}{\hbar}|H_{p',p}|^2\delta(E_{p'} - E_p) \tag{2.37}$$

where E_p and $E_{p'}$ are the energies of the initial and final states including the perturbation state and ensures the δ-function indicate energy consumption. $H_{p',p}$ is the matrix element of the scattering potential between states p' and p obtained using Fermi's Golden Rule approximation and is given by

$$H_{p',p}(t) = \int_{-L/2}^{L/2} \psi_{p'}(z)U_S(z,t)\psi_p(z)\,\mathrm{d}z \tag{2.38}$$

where ψ_p and $\psi_{p'}$ are wavefunctions associated with the state p and p' respectively, and $U_S(z,t)$ is the time varying perturbation potential.

In the subsequent sections, we will be looking at the scattering mechanisms that are dominant mainly for electrons confined in a two-dimensional system.

2.5.1 Acoustic Phonon Scattering

Because a semiconductor's band structure is determined by the crystal potential it is influenced by changes in lattice spacing. A semiconductor under pressure has a perturbed

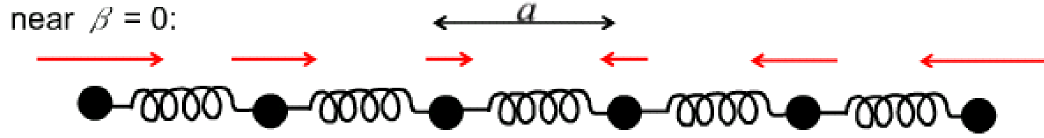

Figure 2.6: Longitudinal acoustic phonons are the crystal vibrations where atoms vibrate along the same direction

lattice constant and band structure. For a small change in lattice constant, we expect that

$$\delta E_C = D_C \frac{\delta a}{a}$$
$$\delta E_V = D_V \frac{\delta a}{a} \tag{2.39}$$

where D_C and D_V, the deformation potentials, can be deduced from experiments and have been characterized for common semiconductors, a is the lattice constant of the semiconductor and δa is the change in lattice constant due to lattice vibrations. The change in effective mass with lattice constant is small and is neglected. Fig. 2.6 illustrates the acoustic phonons in a crystal. Note that the two atoms on the unit cell vibrate along the same direction.

Following the approach given in ref. [22] the momentum relaxation time for longitudinal acoustic phonon scattering in a two-dimensional system is given by

$$S_{p',p} = \frac{1}{\tau_{adp}} = \sum_{m=1}^{m_{max}} \frac{(2+\delta_{m,n})\pi D_A^2 k_B T N(E_k)}{\hbar \rho v_s^2} \tag{2.40}$$

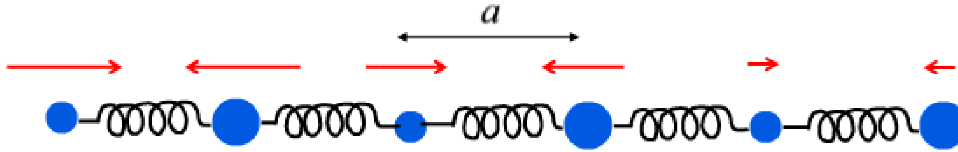

Figure 2.7: Longitudinal polar optical phonons are the crystal vibrations where the atoms vibrate along opposite direction

where $N(E_k)$ is the density of states, *m* and *n* are the initial and final subband numbers respectively, m_{max} is determined by the number of subbands occupied by electrons considering energy absorption after scattering, D_A is the acoustic deformation potential, ρ and v_S are the density and speed of sound in the semiconductor material respectively. In the case of intra-subband scattering within the nth subband, $\delta_{m,n}$ is equal to 1, and this is used for scattering within the ground-state subband. In the case of inter-subband scattering, on the other hand, we have $\delta_{m,n}$ equal to 0. The transverse acoustic (TA) mode of phonons don't perturb the lattice significantly to first order, and hence are neglected here in the analysis.

2.5.2 Polar Optical Phonon Scattering

Phonon scattering in polar semiconductors may occur from either acoustic or optical phonons. Polar acoustic phonon, or piezoelectric scattering is much weaker than optical phonon scattering. Polar optical phonons (POP) scattering, is a very strong scattering mechanism for compound semiconductors like GaAs and similar other III-V compound

semiconductors. It is neither elastic nor isotropic. Fig. 2.7 illustrates the polar optical phonons showing that the two atoms in the unit cell vibrate in opposing motion.

The scattering of electrons by absorption and emission of polar optical phonons in quantized 2D systems has been studied by Price and Ridley [22]. Following the approach given in Ref. [22], the characteristic lifetime for a quantum well of width T_{QW} is given by

$$\frac{1}{\tau_{pop}} = \sum_{m=1}^{m_{max}} \frac{e^2\omega_0}{8\epsilon_p T_{QW} E_k}(n(\omega_0) + \frac{1}{2} \pm \frac{1}{2}) \times \left(2 + \delta_{m,n} - \frac{[(m-n)^2 E_0 \pm \hbar w^*](1+\delta_{m,n})}{[(m-n)^4 E_0^2 + 2(m-n)^2 E_0(2E_k \pm \hbar\omega^*) + (\hbar\omega^*)^2]^{1/2}}\right) - \left(\frac{[(m+n)^2 E_0 \pm \hbar w^*]}{[(m+n)^4 E_0^2 + 2(m+n)^2 E_0(2E_k \pm \hbar\omega^*) + (\hbar\omega^*)^2]^{1/2}}\right) \tag{2.41}$$

where $n(\omega_0) = 1/(\exp(\hbar\omega_0/k_B T) - 1)$ is the phonon occupancy number derived using Bose-Einstein statistics, $\hbar\omega_0$ is the optical phonon energy of the semiconductor. The quantity $\hbar\omega^*$ acts as an effective phonon energy which can be negative and is equal to $\hbar\omega^* = \hbar\omega_0 \pm (n^2 - m^2)E_0$, E_0 is the energy of the ground subband with respect to conduction band edge, E_k is the kinetic energy of the electrons with respect to conduction band edge. In extreme quantum limit (EQL) where only the ground subband is occupied, $m = n$ for absorption and emission. Thus intra-subband scattering is favored over inter-subband scattering. Outside EQL a special case occurs when the difference in energy between two levels is equal to $\hbar\omega_0$, this allows a vertical transition to occur between the minima. Such a transition would be allowed between levels 2 and 1 when $E_0 = \hbar\omega/3$.

2.5.3 Alloy Disorder Scattering

In a compound semiconductor consisting of three or more elements, each of the three elements ie expected not to be periodic in the crystal. As an example let us consider a three-element compound semiconductor such as $A_xB_{1-x}C$; the crystal is usually assumed to consist of $(AC)_x$ and $(BC)_{1-x}$ on average in the ratio x:(1-x). Under this assumption the energy band structure of $A_xB_{1-x}C$ is calculated with the average lattice constant and average pseudopotentials estimated from the ratio x:(1-x). The assumption is called virtual-crystal approximation. This approximation is based on the assumption that the atoms A and B are distributed uniformly in the ratio x:1-x around the cation C. In real alloy compounds it is expected that the distribution is not uniform. This non-uniformity results in a local variation of the periodic potential and this in electron scattering due to the non-uniform potential. This scattering is called alloy scattering.

The relaxation time for alloy scattering can be written as [23]

$$\frac{1}{\tau_{alloy}} = \frac{m^* x(1-x)\Omega V^2}{\hbar^3} b \tag{2.42}$$

where x is the mole-fraction composition of the ternary alloy, V is the alloy disorder scattering parameter, and Ω is the unit cell volume. b is called the Fang-Howard expression [24] of wavefunctions for Hartree approximation and is given by [25]

$$b = \left(\frac{33e^2 m^* n_{2D}}{8\epsilon_0 \epsilon_s \hbar^2} \right)^{1/3} \tag{2.43}$$

Being a short-range potential, the effect of screening by free carriers was neglected.

2.5.4 Remote Ionized Impurity Scattering

The discovery of modulation doping by Dingle et. al. [26] in 1978 has enabled to improve the low-temperature mobility in AlGaAs/GaAs heterostructures. The most important factor to achieve high electron mobility is to separate 2DEG from ionized impurities in modulation-doped AlGaAs/GaAs heterostructures, where the 2DEG in GaAs layer at the interface is supplied from the donors doped in the barrier layer AlGaAs. This structure will reduce ionized impurity scattering because the GaAs layer is not doped intentionally and this very low density of acceptors is introduced unintentionally. At low temperatures 2DEG is suffered from acoustic phonon scattering and ionized impurity scattering. Therefore the ionized impurities introduced in AlGaAs layer are the most important source of electron scattering. Interaction potential of 2DEG with such remote ionized impurities in AlGaAs is long range and expected to be the source of scattering potential for 2DEG in GaAs layer. It is well known that the introduction of a spacer layer, non-doped layer in the barrier AlGaAs at the interface, will increase the electron mobility significantly [27].

The scattering from remote ionized impurities is considered for a two-dimensional sheet of charged impurities, n_{imp}^{2D}, separated from the quantum well by a spacer of thickness d by taking the Fourier transform of the Coulomb potential. The effects of screening are included by using the Thomas-Fermi approximation. The remote ionized impurity scattering rate for a two-dimensional sheet of impurity atoms at d is then

$$\frac{1}{\tau_{rii}} = n_{imp}^{2D} \frac{m^*}{2\pi\hbar^3 k_f^3} \left(\frac{e^2}{2\epsilon_0 \epsilon_s} \right)^2 \int_0^{2k_f} \frac{\exp(-2qd)}{(q+q_{TF})^2} \frac{q^2 dq}{1-\sqrt{(q/2k_f)^2}} \tag{2.44}$$

The bounds of the integral refer to scattering angles between 0 and 180.

2.5.5 Interface Charge Scattering

Since the two-dimensional electron gas is formed at the interface of a wide bandgap material and a narrow bandgap material, there is additional coulomb scattering due to interface charge at the barrier and channel interface.

The corresponding momentum relaxation time is given by [28]

$$\frac{1}{\tau_{int}} = \frac{e^4 m^* N_{int}}{8\pi\hbar^3\epsilon^2 q_F^2} \frac{1}{I_B(\beta)} \tag{2.45}$$

where N_{int} is the 2-d interface charge density per energy and

$$I_B(\beta) = \int_0^\pi \frac{\sin^2\theta \mathrm{d}\theta}{(\sin\theta + \beta)^2} \tag{2.46}$$

where $S_0 = 2e^2m^*/4\pi\epsilon\hbar^2$ is the screening constant [29] and $\beta = S_0/(2q_F)$.

2.5.6 Interface Roughness Scattering

A further source of scattering, which is exclusive to heterostructure systems, comes from variation in the interfaces at the edges of the quantum well. Roughness at these interfaces causes the energy of the confined states to change as the width of the confinement changes. This has been studied in detail by Hong et. al. [30] for a quasitriangular single heterointerface, where a strong dependence on well width is observed. For type-I aligned heterostructures, the dependence of the 2DEG ground-state energy on quantum well dimensions can be considered, to a first approximation, by referring to solutions to the time-independent Schrodinger equation in an infinite square well [31, 32]. The deviation from a perfectly flat interface is described by the function $\Delta(r)$, where r covers the (x,y) plane in which the interface is defined. Δ is the rms average variation in the interface in the z-direction, which is usually of the order of a few monolayers for MBE-

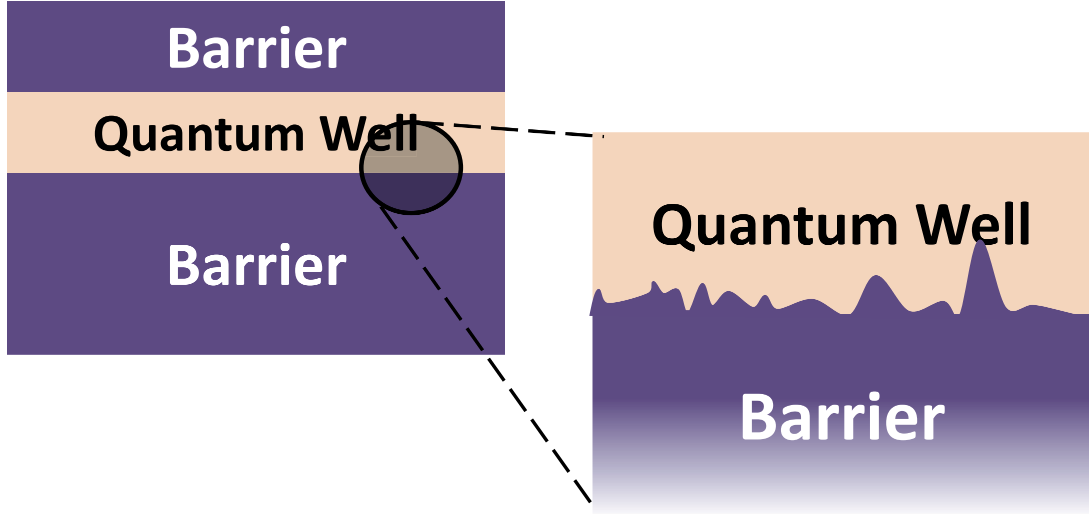

Figure 2.8: Figure showing interface roughness at barrier-QW interface resulting in electron scattering.

grown heterostructures [33], and L is the characteristic extent of the roughness features. These quantities may be found by standard imaging techniques, such as cross-sectional transmission electron microscopy or atomic force microscopy. Fig. 2.8 illustrates the interface roughness at the barrier-QW interface resulting in potential fluctuations causing scattering.

The scattering rate is calculated from the Born approximation by using the square of the interface scattering matrix element given in Refs. [31, 32, 33].

$$|H|^2 = \frac{\pi^5 \hbar^4 \Delta^2 L^2}{m^{*2} T_{QW}^6} \exp\left(-\frac{q^2 L^2}{4}\right) \tag{2.47}$$

where T_{QW} is the thickness of the quantum well. The transport lifetime associated with interface roughness is expressed in terms of the scattering wave vectors as

$$\frac{1}{\tau_{IR}} = \frac{\pi^4 \hbar \Delta^2 L^2}{2m^* T_{QW}^6 k_f^3} \int_0^{2k_f} \exp\left(-\frac{q^2 L^2}{4}\right) \frac{q^2 dq}{1 - \sqrt{(q/2k_f)^2}} \tag{2.48}$$

The transport lifetime in this analysis is extremely sensitive to the well width T_{QW}, so that scattering by interface roughness in wide wells is significantly lower than in narrow wells, which is due to the reduced influence the variation has on the ground state energy E_0. This scattering mechanism potentially has a significant influence on the observed reduction in low-temperature mobility in narrow well samples.

The total mobility can be found from the average transport lifetime in the relaxation time approximation as [34]

$$\mu = \frac{e\langle \tau_{tr} \rangle}{m^*} \tag{2.49}$$

where

$$\frac{1}{\tau_{tr}} = \frac{1}{\tau_{adp}} + \frac{1}{\tau_{pop}} + \frac{1}{\tau_{alloy}} + \frac{1}{\tau_{rii}} + \frac{1}{\tau_{IR}} + \frac{1}{\tau_{int}} \tag{2.50}$$

This is known as Mattheissen's rule and states that the mobility may be deduced from the mobility due to each mechanism acting alone. Mattheissen's rule is often used to estimate mobility when multiple scattering mechanisms are present, but it applied only if the independent scattering mechanisms have the same energy dependence. It is commonly used in practice because it is often easy to estimate the mobility for various scattering mechanisms independently.

Chapter 3

Transport in Mixed Anion As-Sb Quantum Well Heterostructures

3.1 Introduction

In this chapter we discuss the properties of Arsenide-Antimonide quantum well heterostructures with emphasis on low-field transport properties. We first discuss the need and issues that are faced for scaling the QW and barrier thickness. We then dive into the fabrication of the wide and scaled InAsSb quantum well and the hall structure. Band alignment and eigenenergies are simulated using self consistent Schrodinger-Poisson solver (Nextnano) for the scaled and the thick As-Sb quantum well. The transport and confinement effective masses for the quantum well are extracted using simulations and measurements. Next, the sheet charge density in the thick and scaled InAsSb quantum well extracted from Hall measurements is modeled, revealing the subband occupancy. Finally, the low-field electron mobility in the thick and scaled InAsSb QW is modeled by incorporating the scattering mechanisms discussed in the previous chapter.

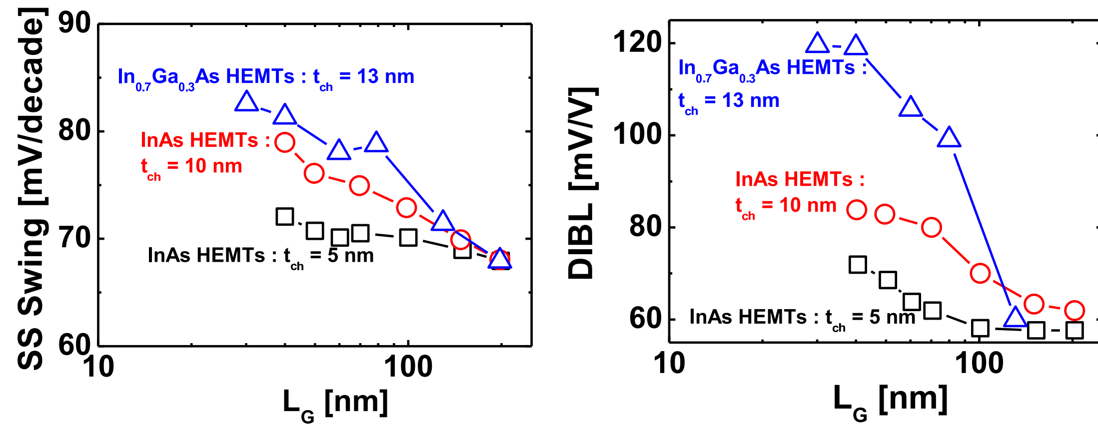

Figure 3.1: Subthreshold swing and DIBL vs. gate length for different QW thickness showing enhanced short channel effects with channel scaling [36]

3.2 Scaling of HEMT

Like in the case of Si MOSFETs, there is no dearth of experimental evidence suggesting the benefits of scaling QW features on HEMT performance. Scaling of quantum well thickness and top insulator or barrier thickness has maximum impact on device performance. Fig. 3.1 shows the subthreshold swing and Drain-induced Barrier Lowering (DIBL) versus gate length of three different quantum well thicknesses [36]. It is evident that the short channel effects are drastically improved with scaling of the QW thickness. Strong electrostatic confinement of electrons in thin quantum well devices pushes the channel conduction subbands to higher energies , which subsequently results in higher

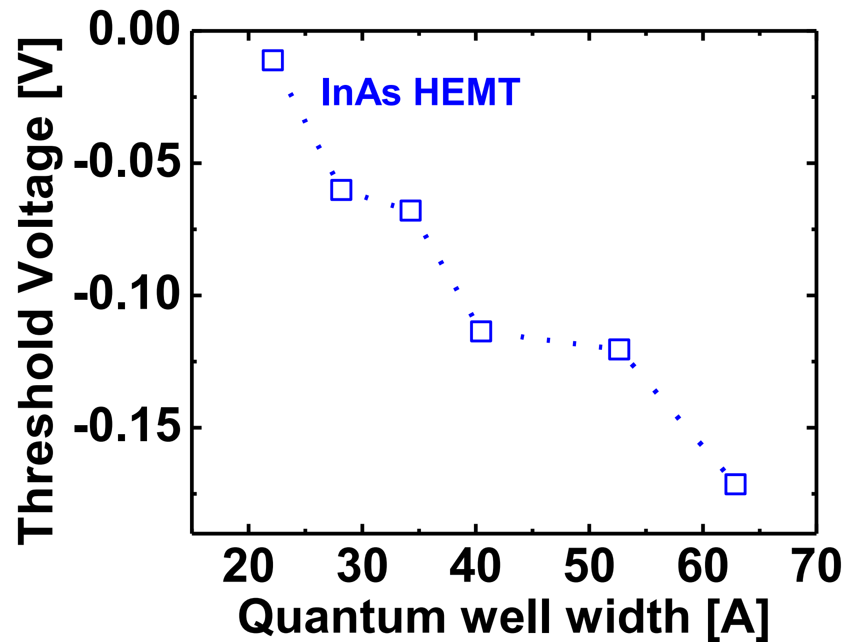

Figure 3.2: Threshold voltage shift as a function of QW width due to increased quantum confinement [37]

V_T and facilitates enhancement mode operation of the devices as shown in Fig. 3.2 [37] The channel effective mass along the transport direction increases as QW thickness scales due to confinement and nonparabolicity of the conduction band as can be seen in Fig. 3.3 [37]. This leads to lower injection velocity but a higher carrier density at the virtual source, resulting in a net increase of current in thin QW channel devices. Increase in confinement effective mass indicates lower quantization in the QW even with sufficiently scaled channel thickness. In order to understand the implications of scaling on low-field mobility, it is essential to correlate effect of scaling on the dominant scattering mechanisms that affect the carrier lifetime. Fig. 3.4 shows the experimental [38] electron hall mobility as a function of QW thickness. Mobility rapidly decreases with QW thickness following T_{QW}^6 power law due to increased interface roughness scattering. Carriers in the thinner QW feel the perturbation in potential from IR much stronger as the wavefunction is closer to the interface as compared to thick QW. Additionally, scal-

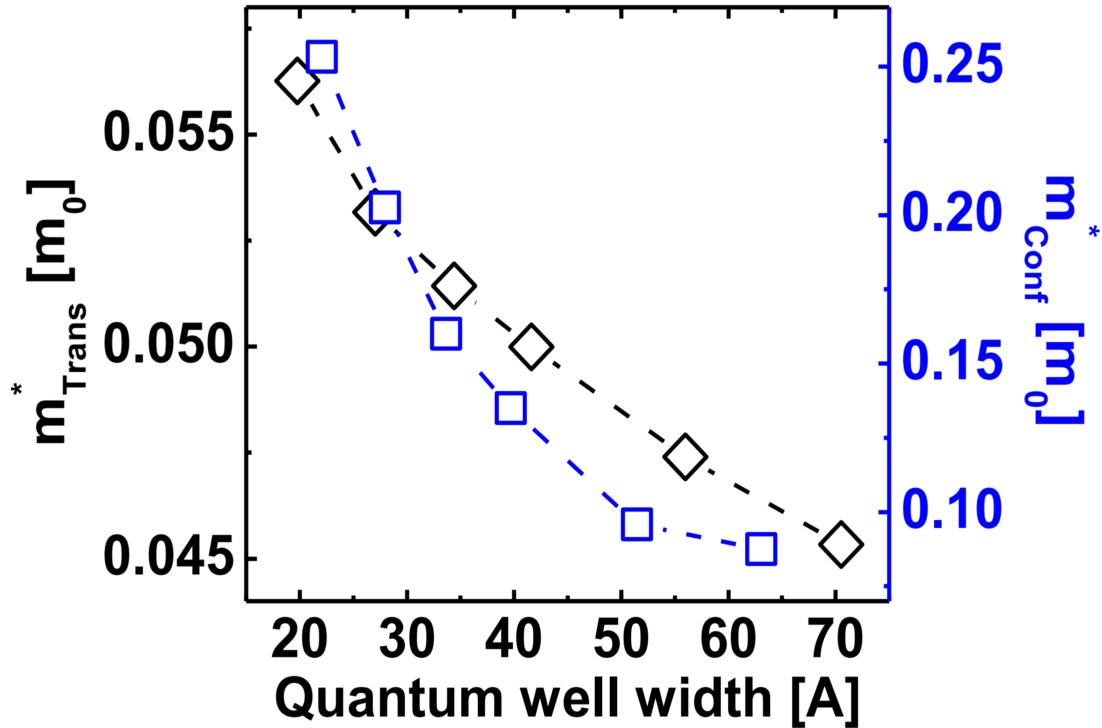

Figure 3.3: Simulated transport and confinement effective mass as a function of QW thickness calculated from tight binding calculations. Effective mass increases due to higher confinement and strong effect of nonparabolicity [37].

ing the top barrier thickness also degrades the mobility due to increased remote ionized impurity scattering from the ionized dopants in the delta-doped barrier.

3.3 As-Sb Heterostructure Band Diagram

Two device structures were fabricated for transport measurements. The schematic of the two structures is shown in Fig. 3.5. The epitaxial layers are grown using Molecular Beam Epitaxy on semi-insulating GaAs substrate. The $Al_{0.8}Ga_{0.2}Sb$ buffer is designed to accommodate the lattice mismatch and to contain the dislocations away from the

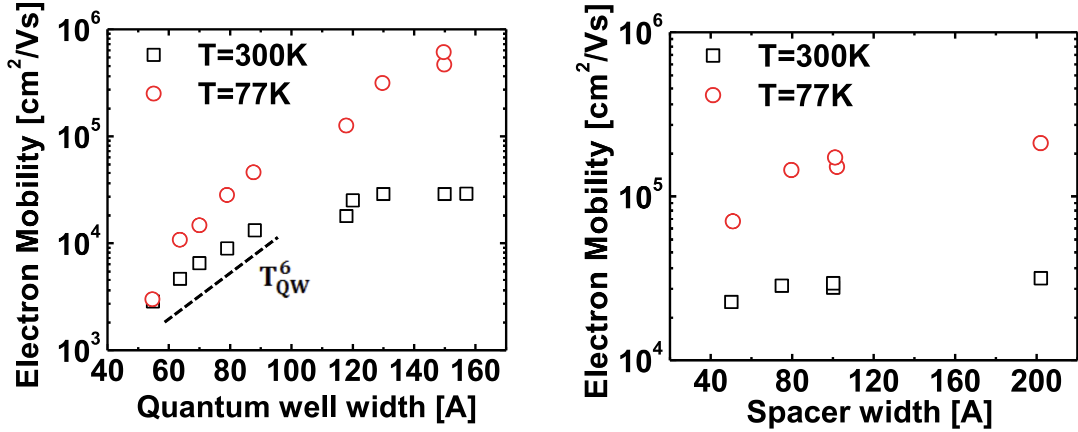

Figure 3.4: Electron Hall mobility as a function of QW and barrier thickness [38].

quantum well. The high quality $\mathrm{InAs_{0.8}Sb_{0.2}}$ quantum well channel was grown on the AlGaSb buffer. $\mathrm{Al_{0.8}In_{0.2}Sb}$ top barrier was deposited on top of the channel. The top barrier was δ-doped using Silicon as n-type dopant. A thin GaSb cap layer is used on top of the barrier for two reasons: to avoid oxidation of Al in the AlInSb top barrier, and because $\mathrm{Al_2O_3}$ forms a very clean interface with GaSb, featuring very low $\mathrm{D_{IT}}$ [35]. $\mathrm{Al_2O_3}$ was deposited on top of GaSb using Plasma-Enhanced Atomic Layer Deposition (PEALD) technique [39].

Device A has $\mathrm{T_{QW}} = 12\mathrm{nm}$ and top barrier $\mathrm{T_b} = 9\mathrm{nm}$. Device B has scaled dimensions with $\mathrm{T_{QW}} = 7.5\mathrm{nm}$ and $\mathrm{T_b} = 5\mathrm{nm}$. The equilibrium band diagram for the scaled and thick InAsSb QW is shown in Fig. 3.6. We see that the $\mathrm{InAs_{0.8}Sb_{0.2}}$ quantum well

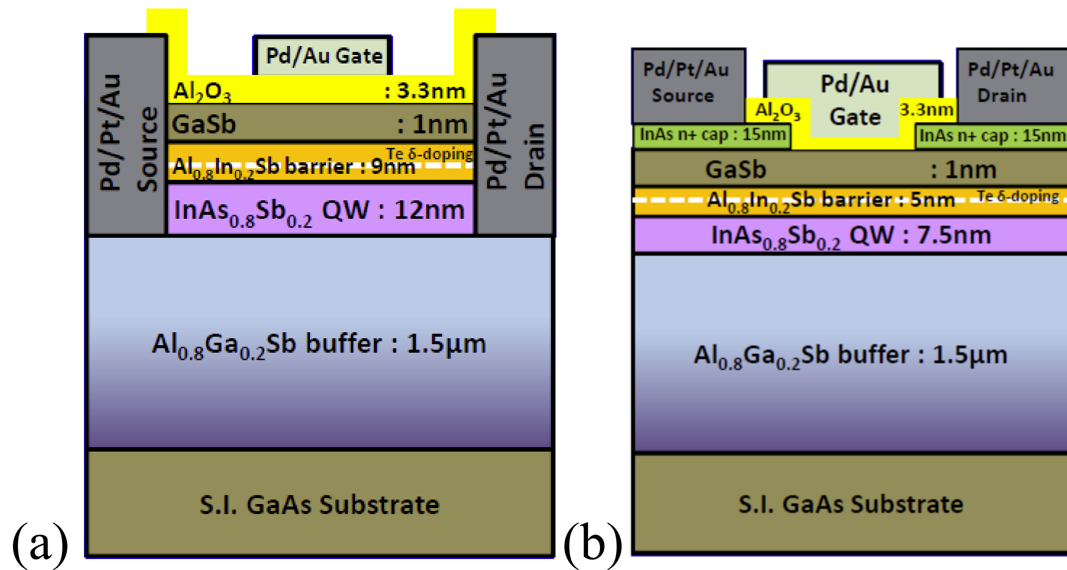

Figure 3.5: Schematic of the $\mathrm{InAs_{0.8}Sb_{0.2}}$ MOS-QWFET on GaAs substrate (a) with 12nm quantum well thickness and 9nm barrier layer, (b) with scaled 7.5nm quantum well thickness and 5nm barrier thickness.

forms a type I band alignment with $\mathrm{Al_{0.8}In_{0.2}Sb}$ top barrier. The fermi level is pinned at 0.1 eV near the valence band edge in GaSb.

3.4 Hall Effect Measurement

A customary technique for determining electron mobility is Hall analysis. Because of its simplicity and low-cost, it is the most commonly used characterization technique for III-V semiconductor heterostructures. This technique determines sheet density ($\mathrm{n_s}$), bulk carrier density (n, p), electron mobility (μ) and sheet resistance ($\mathrm{R_s}$) in semiconductor

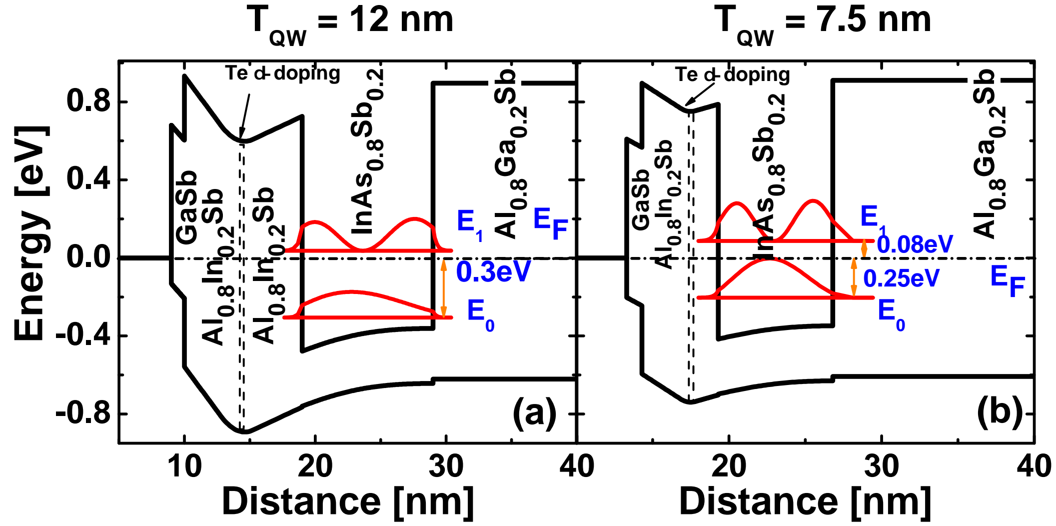

Figure 3.6: Band diagram of $InAs_{0.8}Sb_{0.2}$ quantum well heterostructure with 12nm and 7.5nm quantum well thickness and 1nm GaSb interfacial layer from Schrodinger-Poisson simulation indicating strong electron confinement

samples. The electronic properties are measured using a combination of measurements. The resistivity measurement determines the sheet resistance and the Hall measurements determine the electron mobility and sheet density.

The transverse voltage is known as the Hall voltage V_H and its magnitude is equal to IB/ned, where I is the applied current, B is the applied magnetic field intensity, d is the sample thickness and e is the electron charge. In order to obtain sheet density instead of bulk density, we use

$$n_s = \frac{IB}{q|V_H|} \tag{3.1}$$

Thus by measuring the Hall voltage V_H and from the known values of I, B and e, we determine the sheet density n_s in the InAsSb quantum well.

The sheet resistance R_S of the 2DEG was conveniently determined by the use of Van der Pauw resistivity measurement technique. Since sheet resistance involves both

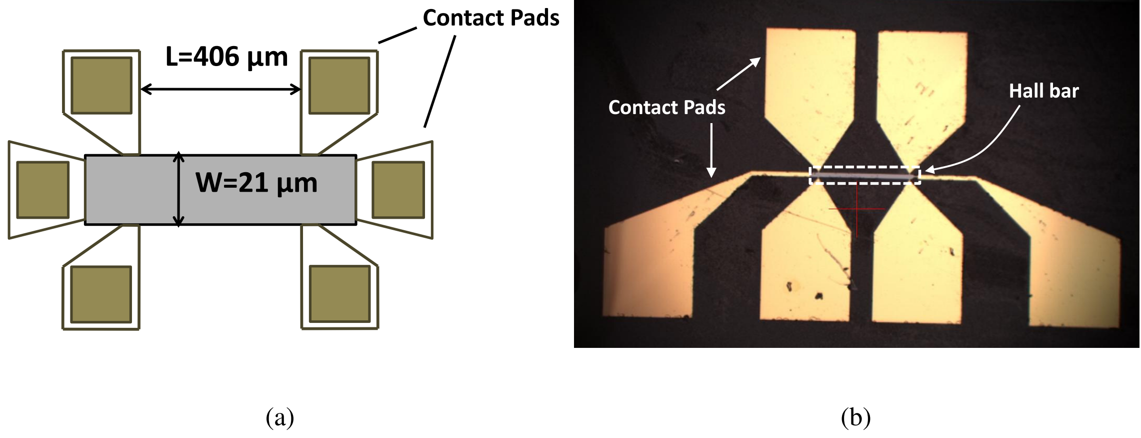

(a) (b)

Figure 3.7: (a)Schematic and (b) Die shot of the hall structure fabricated on the wide and scaled quantum well heterostructures for performing hall measurements from temperature ranging from 4K to 300K

sheet density and mobility, we determined Hall mobility from the following equation

$$\mu = \frac{|V_H|}{R_S I B} = \frac{1}{q n_s R_S} \tag{3.2}$$

Fig. 3.7a shows the schematic of the hall structure fabricated for performing hall measurement to obtain sheet charge density and carrier mobility. The width of the device under test was $21\mu\mathrm{m}$ and length was $406\mu\mathrm{m}$.

3.5 Hall Sheet Charge Density

Fig. 3.8 shows the experimental and modeled electron sheet density as a function of temperature for $\mathrm{T_{QW}} = 12\mathrm{nm}$ and $\mathrm{T_{QW}} = 7.5\mathrm{nm}$ obtained from Hall measurements. We find that the electron sheet density is almost constant, showing a slight decrease with decreasing lattice temperature.

The model developed in Section 2.3 for the 2D sheet charge density in *j*th subband

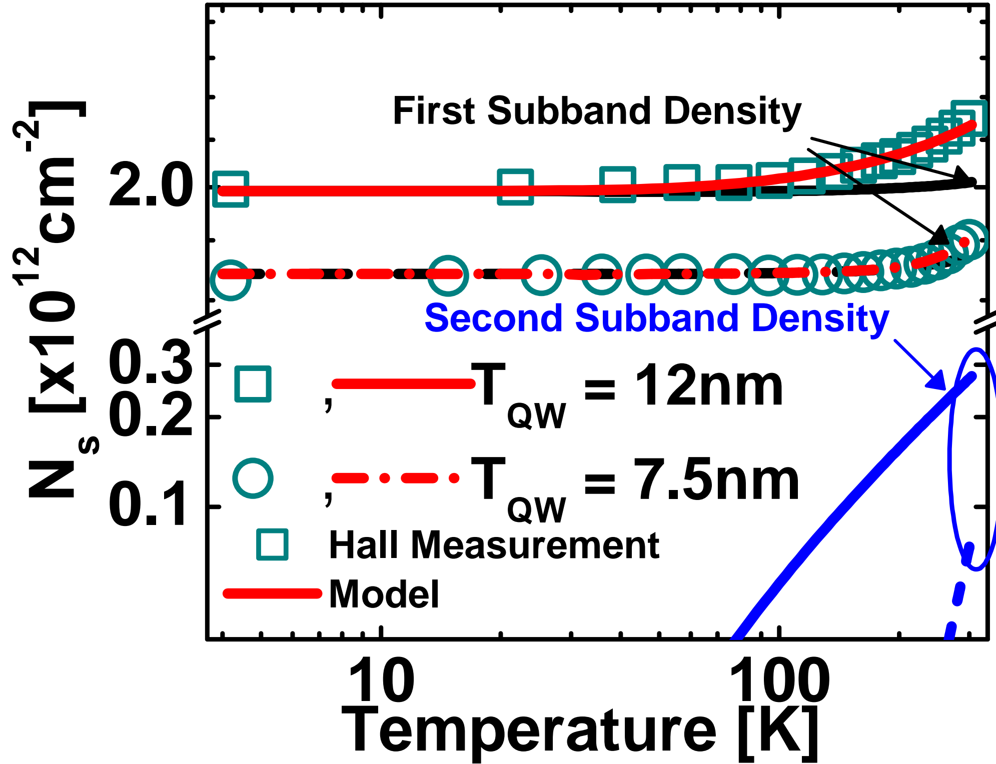

Figure 3.8: Experimental and modeled sheet charge density versus temperature in $InAs_{0.8}Sb_{0.2}$ quantum well channel for 12nm and 7.5nm quantum well thickness. The contribution from ground and first subband is indicated.

incorporating the effect of conduction band nonparabolicity was employed. We find that, for $T_{QW} = 12nm$, the electron sheet density in ground subband is almost constant increasing slightly at higher temperature. Whereas, the electron density in first subband decreases with decreasing temperature. Ground subband is degenerate throughout the temperature range.

Similar results are observed for sample with $T_{QW} = 7.5nm$, with room temperature and low temperature sheet densities reduced due to reduced degeneracy as a result of quantization. The energy of ground and first subband are increased as a result of structural quantization. The ground subband is degenerate throughout the entire temperature range.

The effective mass was changed in the database file of Nextnano (database.in) in order to model the sheet charge density at room and low temperature by adjusting the energy position of ground and first subband with respect to conduction band edge.

These self-consistent results are used for the calculation of the temperature dependence of electron mobility. In the calculation, we use the electron sheet density determined from the Hall measurements, and therefore the total sheet electron density is the same as the experimental value.

3.6 Low Field Mobility in Scaled As-Sb QW

A basic mobility characteristic of the modulation-doped quantum well structure, which reveals the relative importance of the various scattering mechanisms, is the temperature dependence of the electron mobility. To see the importance of different scattering mechanisms in determining the total 2DEG mobility in the AlInSb/InAsSb quantum well heterostructure, we first calculate the temperature dependence of the electron mobility in the modulation-doped quantum well.

In Fig. 3.9, experimental electron mobility for $\mathrm{T_{QW}} = 12\mathrm{nm}$ and $\mathrm{T_{QW}} = 7.5\mathrm{nm}$ are plotted as a function of temperature varying from 4K to 300K. It can be clearly observed that the electron mobility for $\mathrm{T_{QW}} = 7.5\mathrm{nm}$ is degraded by 58% as compared to $\mathrm{T_{QW}} = 12\mathrm{nm}$. To identify clearly the reason for degradation, we break down the electron Hall mobility into various scattering mechanisms as discussed in Section 2.5. Fig. 3.9 also shows the electron mobility and modeled scattering mechanisms for the thick and scaled quantum wells. The material parameters used as input to the mobility model is summarized in Table 3.1.

As we can see from Fig. 3.9 for $\mathrm{T_{QW}} = 12\mathrm{nm}$, at very low temperatures the 2DEG mobility is limited by interface charge scattering and remote ionized impurity scattering.

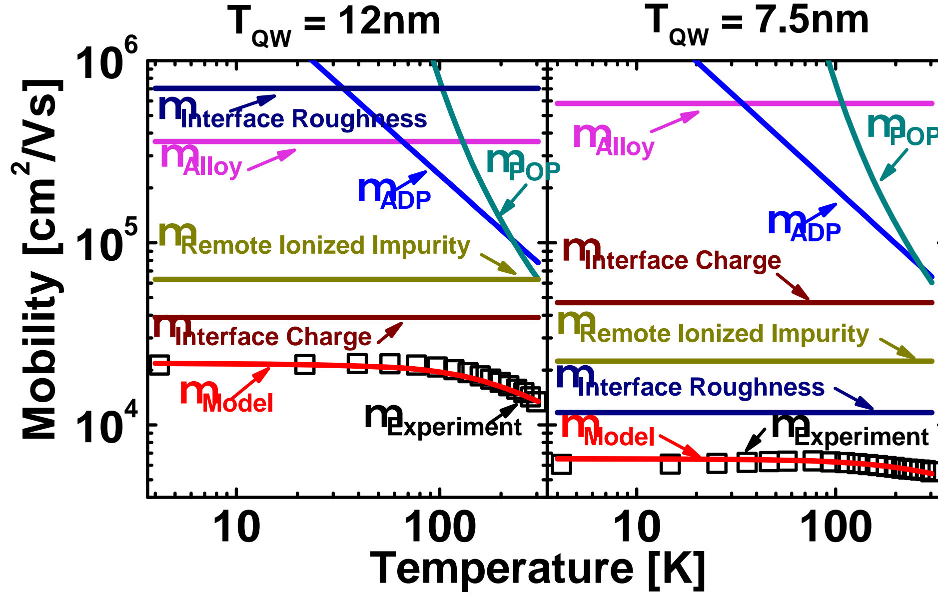

Figure 3.9: Experimental and modeled electron mobility vs. temperature in InAsSb quantum well channel of 12nm and 7.5nm thickness, depicting dominant scattering mechanisms at low and room temperature.

Parameter	Value
Acoustic Deformation Potential	4.8 eV
Polar Optical Phonon Energy	27.8 meV
Alloy Disorder Potential	0.3 eV
Interface Charge	6x10^{11} $/cm^2$
Mean Height of Roughness	6.2A ($T_{QW} = 12nm$) 6.8A ($T_{QW} = 7.5nm$)
Correlation Length	20 nm
Remote Ionized Impurity	1.8x10^{12} $/cm^2$

Table 3.1: Values of different parameters used for scattering rate calculation using Relaxation time approximation

At room temperature there is negative gradient of mobility with temperature, characteristic of phonon scattering limited mobility. Both intra- and inter-subband scattering has been taken into account for acoustic and polar optical phonon scattering, due to significant contribution of electrons from the first subband at room temperature. Alloy scattering and interface roughness scattering cause negligible degradation.

For the device with $T_{QW} = 7.5nm$ and $T_{barrier} = 5nm$, the interface roughness scattering increases by 75x, the remote ionized impurity scattering increased by 3x due to re-

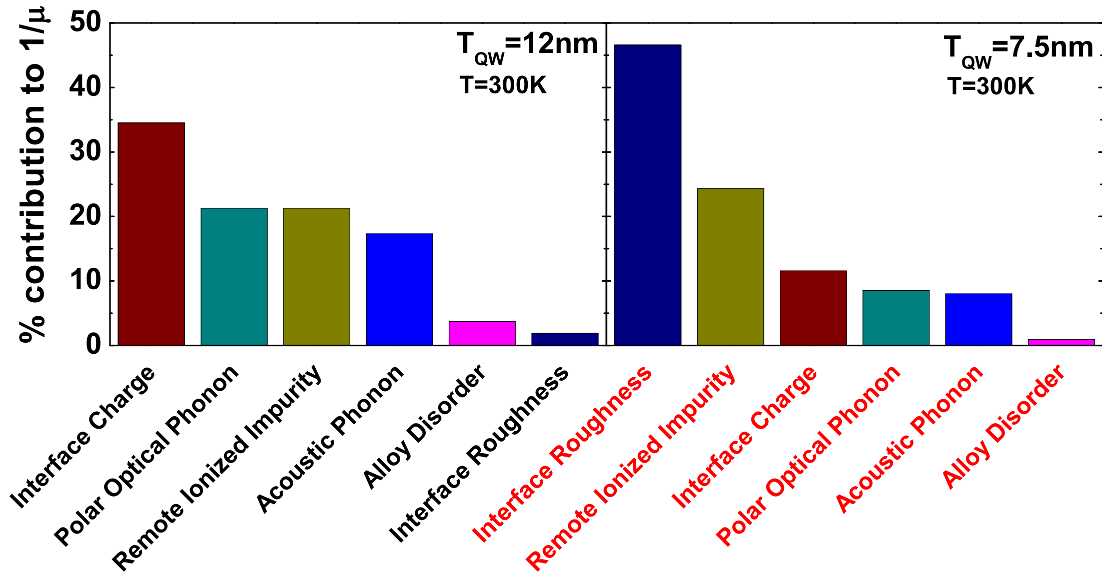

Figure 3.10: Pareto plot showing % contribution of different scattering mechanisms to total mobility at 300K for thick and scaled QW. Interface charge scattering dominates for $\mathrm{T_{QW}} = 12\mathrm{nm}$ and interface roughness scattering dominates for $\mathrm{T_{QW}} = 7.5\mathrm{nm}$.

duction in spacer layer thickness. With increasing well width, the electron wave function spreads across the well and the average distance from the 2DEG to the remote impurities increases, which leads to a decrease of remote doping scattering rate. The random potential for interface-roughness scattering is proportional to $\mathrm{T_{QW}^{-6}}$, so the interface roughness limited mobility increases rapidly with the increase of the well width. Fig. 3.10 plots the % contribution of different scattering mechanisms at 300K for $\mathrm{T_{QW}} = 12\mathrm{nm}$ and $\mathrm{T_{QW}} = 7.5\mathrm{nm}$, asserting the argument regarding dominant scattering mechanisms for the two devices.

3.7 Quantitative Mobility Spectrum Analysis

For modern semiconductor heterostructures containing multiple populations of distinct carrier species, conventional Hall and resistivity data acquired at a single magnetic field provide far less information than measurements as a function of magnetic field. However, the extraction of reliable and accurate carrier densities and mobilities from the field-dependent data can present a number of difficult challenges, which were never fully overcome by earlier methods such as the multi-carrier fit, the mobility spectrum analysis by Beck and Anderson, and the hybrid mixed-conduction analysis. In order to overcome the limitations, an approach described by Antoszewski et. al. [40] and known as Quantitative Mobility Spectrum Analysis (QMSA), has been employed. The algorithm is analogous to a fast Fourier Transform, in that it transforms from the magnetic field B domain to the mobility domain. QMSA converts the field-dependent Hall and resistivity data into a visually-meaningful transformed output, comprising the conductivity density of electrons and holes in the mobility domain.

For the fabricated InAsSb Hall sample, the longitudinal and transverse conductivity tensor components σ_{xx} and σxy, respectively, can be expressed as a sum over the *m* species present within the multi-carrier system [41],

$$\sigma_{xx}(B) = \frac{1}{\rho(B)\{[R_H(B)B/\rho(B)]^2 + 1\}} = \sum_{i=1}^{m} \frac{en_i\mu_i}{1 + (\mu_i B)} \tag{3.3}$$

$$\sigma_{xy}(B) = \frac{R_H(B)B/\rho(B)}{\rho(B)\{[R_H(B)B/\rho(B)]^2 + 1\}} = \sum_{i=1}^{m} S_i \frac{en_i{\mu_i}^2 B}{1 + (\mu_i B)^2} \tag{3.4}$$

where B is the applied magnetic field in the perpendicular direction, $R_H(B)$ and $\rho(B)$ are the experimental magnetic field dependent Hall coefficient and resistivity, respectively, n_i and μ_i are the concentration and mobility of the *i*th carrier species, respec-

tively, and S_i is +1 for holes and -1 for electrons. It is primarily the $(1 + \mu^2 B^2)$ terms in the denominators which separate the contributions from the various carrier species.

The starting point for the QMSA procedure is to allow for the existence of a semi-continuous mobility distribution of hole-like and electrons-like species [42],

$$\sigma_{xx}(B_j) = \sum_{i=1}^{n} \frac{S_i^{xx} \Delta\mu_i}{1 + {\mu_i}^2 {B_j}^2} = \sum_{i=1}^{n} \frac{[s^p(\mu_i) + s^n(\mu_i)]\Delta\mu_i}{1 + {\mu_i}^2 {B_j}^2} \tag{3.5}$$

$$\sigma_{xy}(B_j) = \sum_{i=1}^{n} \frac{S_i^{xy} \mu_i B_j \Delta\mu_i}{1 + {\mu_i}^2 {B_j}^2} = \sum_{i=1}^{n} \frac{[s^p(\mu_i) - s^n(\mu_i)]\mu_i B_j \Delta\mu_i}{1 + {\mu_i}^2 {B_j}^2} \tag{3.6}$$

where $s^n(\mu_i)$ and $s^p(\mu_i)$ are the conductivity density functions i.e. the mobility spectra for electrons and holes, and the parameter *n* defines the number of points in the final mobility spectrum. The resulting spectra of QMSA allows the carrier concentration and mobility to be evaluated for each carrier species. Fig. 3.11 presents the QMSA for the thick and scaled InAsSb QW heterostructure measured at 77K, 200K and 300K, and in the magnetic field ranging from 0T to 9T. One electron peak is clearly resolved with a mobility of 13,300 $\mathrm{cm^2/Vs}$ at 300K and increasing upto 21,000 $\mathrm{cm^2/Vs}$ for 77K for wide QW. Similar trend is observed for scaled QW where one electron peak is clearly resolved with a mobility of 5,500 $\mathrm{cm^2/Vs}$ at 300K and 6,800 $\mathrm{cm^2/Vs}$ at 77K. The absence of other dominant peaks confirm that there is no parallel conduction in the QW layers, and the QW is the only major source of conduction from source to drain.

3.8 Effective Mass

The transport effective mass has been experimentally verified for $\mathrm{T_{QW}} = 12\mathrm{nm}$ by analysis of Shubnikov-de Haas (SdH) effect measured on the device. The SdH magneto-transport measurements were performed at low temperature (2-15 K) and high magnetic

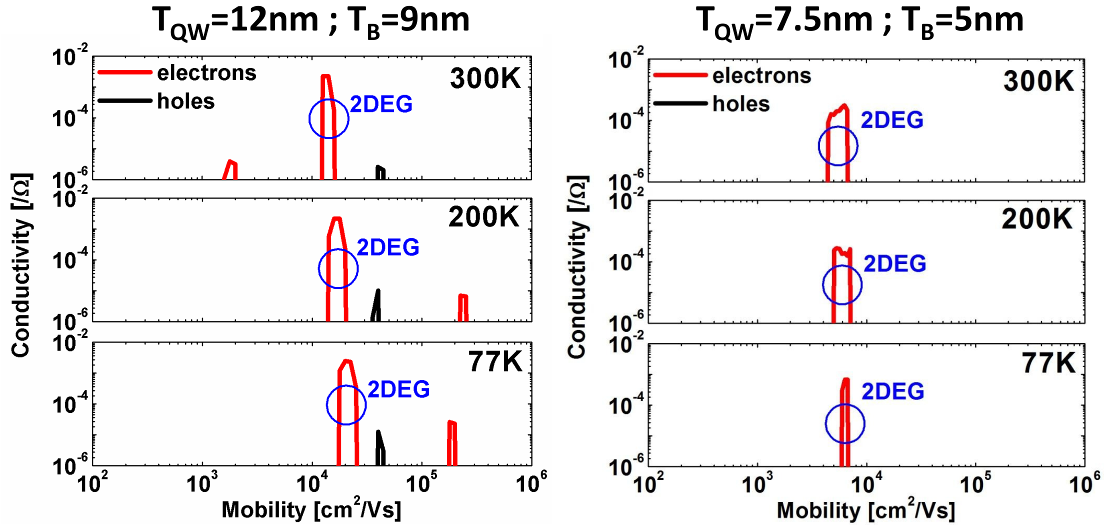

Figure 3.11: Quantitative Mobility Spectrum Analysis for thick and scaled InAsSb Quantum Well heterostructure for 77K, 200K and 300K and magnetic field ranging from 0T to 9T showing one electron peak corresponding to 2DEG in the QW. This indicates absence of parasitic parallel conduction in the semiconductor layers.

field (0-9 T). The magnetotransport measurements, in standard four-probe DC configuration, were carried out using Quantum Design Model 6000 Physical Property Measurement System, with a base temperature of 1.8K and magnetic field in the range of 0-9T. Fig. 3.12 shows the measured sheet resistance (R_{XX}) and Hall resistance (R_{XY}) of the device from 0 to 9 T. The insets in the figures show the configurations to measure R_{XX} and R_{XY}. SdH oscillations are observed in R_{XX} at magnetic fields below 8 T. At fields above 8 T, the quantum Hall plateaus appear in R_{XY}, and R_{XX} tends to zero resistance [43].

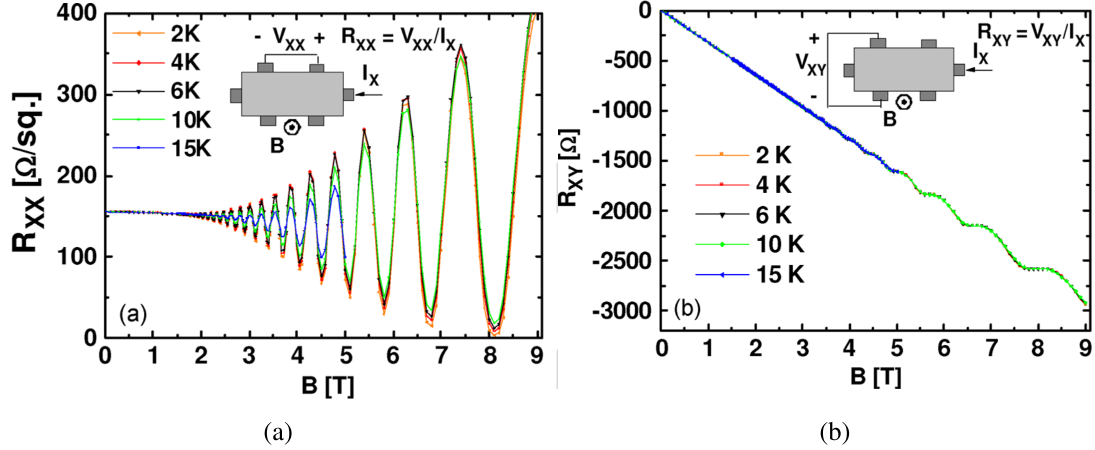

(a) (b)

Figure 3.12: (a) Measured sheet resistance $\mathrm{R_{XX}}$ and (b) Hall resistance $\mathrm{R_{XY}}$ of the InAsSb QW heterostructure from 0-9 T. Insets in the figures show the configurations employed to measure $\mathrm{R_{XX}}$ and $\mathrm{R_{XY}}$

The magnetic field and temperature dependence of sheet resistance can be expressed as [44]

$$\frac{\Delta\rho_{XX}}{\rho_0} = R_S \frac{4\chi}{\sinh\chi} exp\left(\frac{-\pi}{\omega_c\tau_q}\right)\cos\left(2\pi\frac{E_F}{\hbar\omega_c}+\phi\right) \tag{3.7}$$

where ρ_0 is the sheet resistance at zero B, τ_q is the quantum lifetime, $\chi = 2\pi^2 kT/\hbar\omega_c$, and $\omega_c = eB/m^*$ is the cyclotron frequency. The prefactor R_S is associated with Zeeman splitting and is assumed to be independent of the magnetic field in the following analysis. From Eq. (3.7), a plot of $\ln(\Delta\rho_{XX}/\rho_0)$ versus $\ln(\chi/\sinh\chi)$ gives a straight line with slope=1. $\ln(\Delta\rho_{XX}/\rho_0)$ is from the experimentally measured magnetoresistance data as a function of temperature, and $\ln(\chi/\sinh\chi)$ is calculated as a function of temperature using m^* as an adjustable parameter. The correct value of m^* gives a slope of 1 for the graph. Fig. 3.13 shows the extraction procedure at B=2.54 T and B=3.01 T. The extracted effective mass from the analysis is $0.043m_0$ at a sheet carrier density of $2.01\times10^{12}\,\mathrm{cm^{-2}}$ (from the period of SdH oscillations).

For the device B with $\mathrm{T_{QW}} = 7.5\mathrm{nm}$, first the DOS effective mass was estimated by

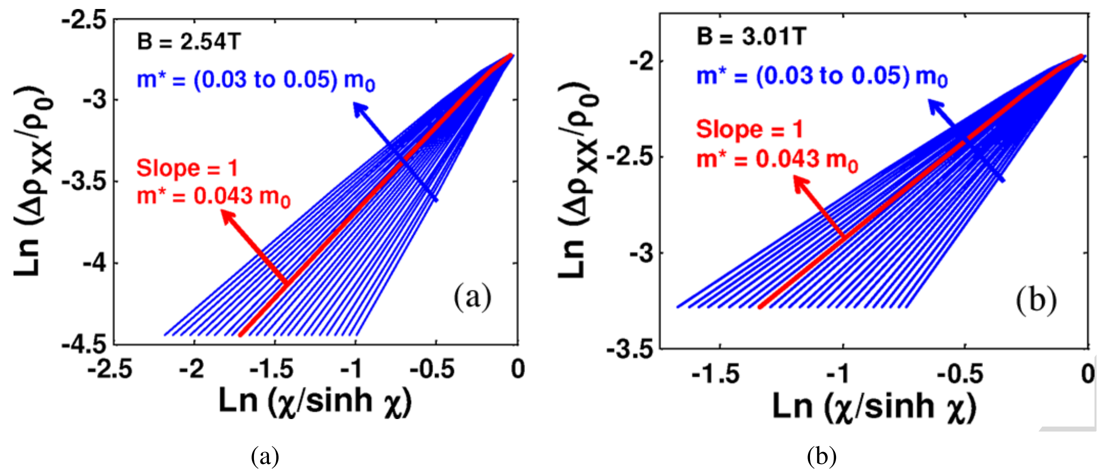

(a) (b)

Figure 3.13: Plot of $\ln(\Delta\rho_{XX}/\rho_0)$ versus $\ln(\chi/\sinh\chi)$ for (a) B=2.54 T and (b) B=3.01 T to extract effective mass. Correct value of effective mass gives a slope of 1 for the graph

fitting the sheet charge density, and the transport effective mass was correlated. Fig. 3.14 summarizes the confinement and transport effective mass as a function of quantum well width. This clearly signifies the effect of nonparabolicity in confinement and transport direction. It is noticeable that the nonparabolicity effect in the confinement direction is much more prominent than in the transport direction as the quantum well width is scaled.

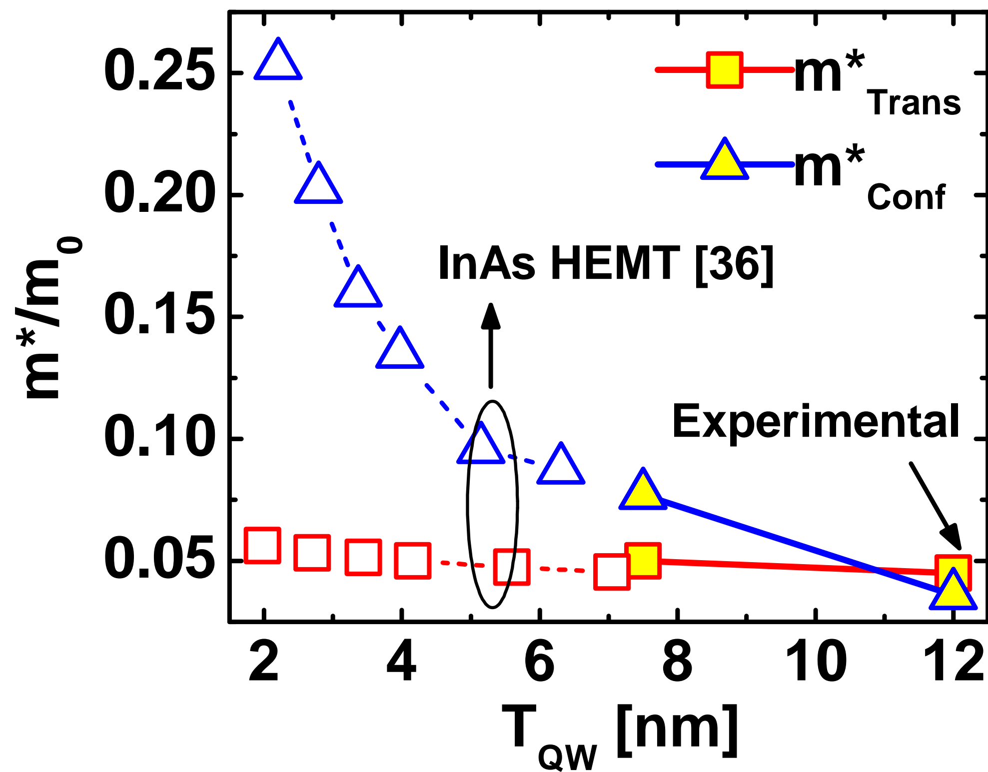

Figure 3.14: Transport and confinement effective mass as a function of quantum well width in InAsSb quantum wells. The effect of nonparabolicity is more prominent in the confinement direction resulting in large increase in eff. mass for $\mathrm{T_{QW}} = 7.5\mathrm{nm}$. For reference, effective mass for InAs HEMT [37] has been shown for ultra scaled QW thickness.

Chapter 4

Conclusions

In this thesis, we have developed a simple analytical model for low-field transport for Arsenide-Antimonide based quantum well heterostructures. We analyzed experimental hall sheet density and hall electron mobility on As-Sb QW MOSHEMT. Our model explains cogently, the various dominant scattering mechanisms for the wide and scaled QWs. In this chapter, key findings of this analysis work are briefly summarized.

In this work, we explain the low-field transport in Arsenide-Antimonide quantum well heterostructures. The 6.2A semiconductor has many potential advantages owing to its narrow band-gap, low effective mass and consequently low mobility. The experimental InAsSb quantum well heterostructures studied in this work have two different types of device structures which include different (5 and 9nm) barrier thickness and (7.5 and 12nm) channel thickness. We fabricated a hall structure on the two device layers, and extracted sheet charge density and electron mobility from Hall measurements with temperature ranging from 4K to 300K.

Band structure of AlInSb/InAsSb heterostructure was simulated using a Schrodinger Poisson solver (Nextnano) for wide and scaled quantum wells. Subband position and fermi level were calculated based on the sheet charge density measured using hall mea-

surements. Effect of nonparabolicity was found to be significant in confinement and transport direction in the E-k space, owing to the narrow bandgap of InAsSb semiconductor. The transport effective mass for $\mathrm{T_{QW}} = 12\mathrm{nm}$ was measured experimentally and nonparabolicity factor of $\alpha = 2.5\,/\mathrm{eV}$ was extracted. Nonparabolicity in confinement mass was estimated by fitting the sheet charge density measured experimentally using hall measurement for the wide and scaled quantum wells. The model very well captures the experimental hall sheet charge density in wide and scaled InAsSb quantum well.

Additionally, we have built a physical electron Hall mobility model based on Boltzmann Transport formalism that incorporates various relevant and dominating scattering mechanisms in III-V HEMTs. The scattering mechanisms identified to be of significance are: Acoustic deformation potential scattering, polar optical phonon scattering, remote ionized impurity scattering, interface charge scattering, alloy disorder scattering and interface roughness scattering. The model efficiently explains the low-field electron transport in the high mobility mixed anion Arsenide-Antimonide quantum well heterostructures.

For device A with $\mathrm{T_{QW}} = 12\mathrm{nm}$, we find that major contribution to the charge carriers comes from the ground subband, first subband contributes upto 10% near room temperature. The effect of nonparabolicity was incorporated in the mobility calculations by using the transport effective mass obtained experimentally using Shubnikov-de Haas oscillations. We conclude that the dominant source of scattering for limiting electron mobility is coulomb scattering from interface charge at the barrier/channel interface and from remote ionized impurity from the delta doping in the AlInSb top barrier separated from the 2DEG by a thin spacer layer. Acoustic and polar optical phonon scattering plays a significant role at room temperature. Intra- and inter-subband scattering has been accounted for to calculate phonon-limited mobility. Hence, in order to im-

prove low-field mobility, it is imperative to significantly reduce the density of interface charge at the barrier/channel interface. Additionally, improvement can be achieved by reducing remote ionized impurity scattering, either by reducing δ-doping or by increasing the spacer thickness between δ-doping and the channel. The intrinsic performance is expected to be limited by Alloy disorder scattering at low temperatures and phonon scattering at room temperatures.

For device B with $\mathrm{T_{QW}} = 7.5\mathrm{nm}$ and $\mathrm{T_{barrier}} = 5\mathrm{nm}$, the quantization effect reduces but still limits the contribution to the ground subband, first subband contributes only at higher temperatures. We see that the low-field mobility is degraded by 2.4x as compared to wide quantum well device. The transport effective mass was calculated assuming the same nonparabolicity factor for the scaled quantum well, and was used in the mobility calculations. Analysis of the scattering mechanisms shows that interface roughness scattering and remote ionized impurity scattering are the dominant scattering mechanisms limiting the mobility at low and room temperature. The modulation of mobility with temperature is very insignificant, asserting that phonon scattering does not affect mobility significantly. In order to improve the mobility, we need to reduce the interface roughness between the barrier and the channel interface. Next, mobility can be improved by increasing the spacer thickness between δ-doping and the 2DEG to reduce remote ionized impurity scattering.

Based on the conclusions drawn above, solutions can be suggested by which performance of the QW MOSHEMTs can be improved.

Orientation : Exploring transport properties for different channel directions is essential. Moschetti et. al [45] have studied the effect of channel orientation on the low field mobility and have demonstrated interesting results. Anisotropic transport in InAs/AlSb HEMTs grown on (001) InP substrates has been studied. 32% lower sheet resistance is observed along the [1-10] direction compared to [110] direction. Study of low field mo-

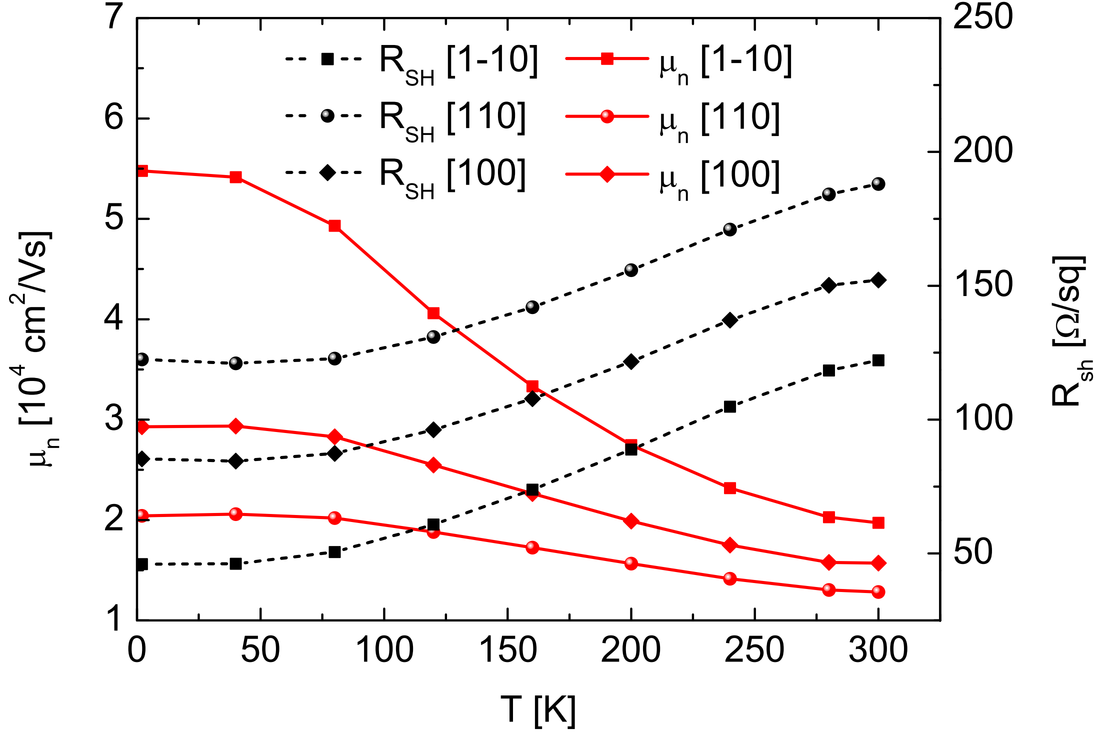

Figure 4.1: Electron hall mobility vs. temperature for InAs/AlSb QW for different channel directions showing enhanced anisotropy in [1-10] direction [45].

bility as a function of temperature for various channel directions (Fig. 4.1) showed that the anisotropy was enhanced with reducing temperature, due to reduced polar optical phonon scattering at low temperature. The anisotropic transport was found to be related to the presence of threading dislocations in the AlSb metamorphic buffer.

We can envision a schematic for future As-Sb QW MOSFET structure as shown in Fig. 4.2. It features the InAsSb quantum well channel layer and a thin high-k dielectric layer on top of the interfacial GaSb layer to form an interface with low D_{IT}. Source and drain regions are self aligned and highly doped n+ to reduce the ohmic contact resistance. A δ-doping layer is implemented on the bottom buffer layer. It is optimized so that there are sufficient carriers in the QW channel region and to realize enhancement

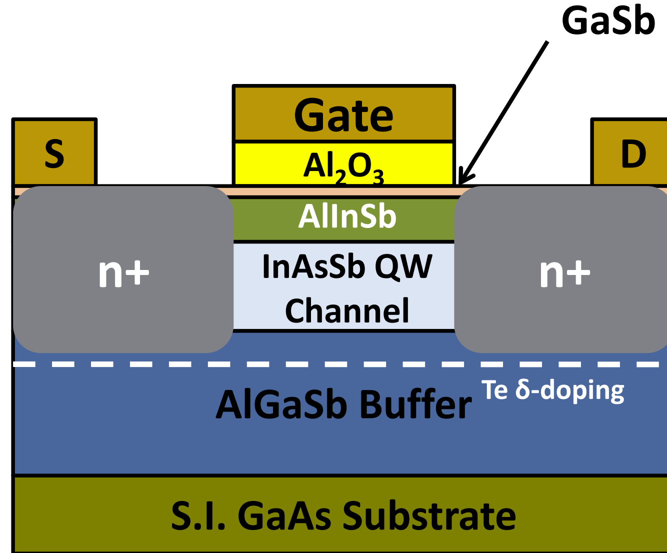

Figure 4.2: Schematic of a future As-Sb QW MOSFET structure.

mode operation. The source drain implant allow us to reduce δ-doping without worrying about access resistance. The undoped QW channel layer enables carriers to have higher velocity due to reduced scattering and high mobility of the InAsSb channel material.

If all the design and performance challenges are met, the III-V MOSHEMT is a viable candidate for future technology nodes, especially below $\mathrm{L_G} = 10nm$. It is absolutely essential that we scale the HEMT features i.e. the QW thickness and the insulator width in order to prevent performance degradation due to short channel effects, and to achieve lower EOT for higher $\mathrm{I_{ON}}$. Based on the calculations it is estimated that for $\mathrm{L_G} = 10nm$ device, the desired QW thickness would be $\mathrm{T_{QW} = 3nm}$ and the insulator thickness would be $\mathrm{T_b = 2.5nm}$. Fig. 4.3a shows the calculated hall mobility and the various scattering mechanisms as a function of temperature for the ultimately scaled device. We calculate a mobility of 770 $\mathrm{cm^2/Vs}$ at 300K. The transport is dominated by interface roughness scattering, and shows no modulation with temperature. For $\mathrm{T_{QW} = 3nm}$ only the ground subband will be occupied (extreme quantum limit).

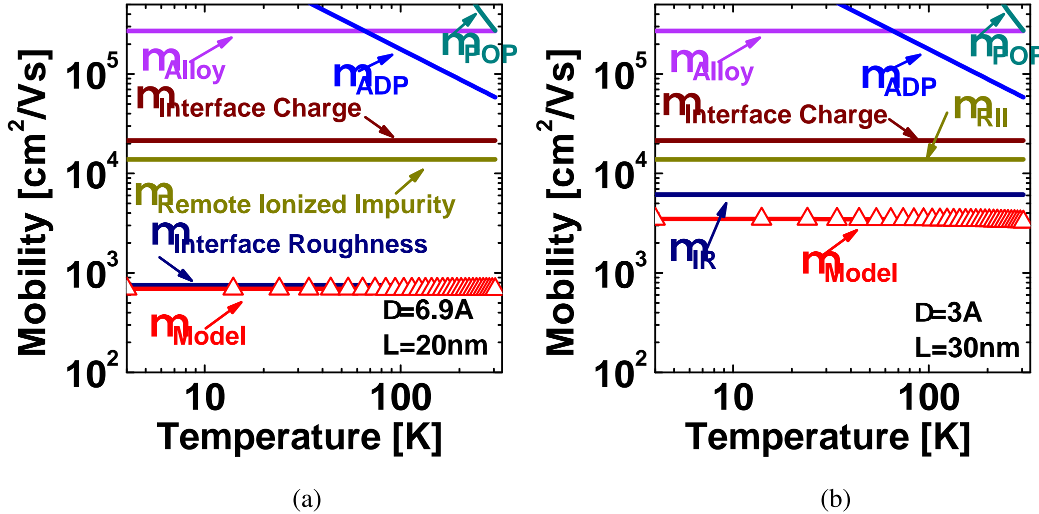

(a) (b)

Figure 4.3: (a) Calculated electron mobility and scattering mechanisms as a function of temperature for $\mathrm{T_{QW}} = 3\mathrm{nm}$, (b) calculated electron mobility as a function of temperature with reduced mean height of roughness and increased correlation length, showing improved performance.

Hence the reduction in intersubband scattering leads to increased POP limited mobility.

The calculated mobility is pretty low and would be a concern for drive current degradation. It is essential that we reduce the interface roughness, in order to improve the mobility. Fig. 4.3b shows the calculated mobility for $\Delta = 3\mathring{A}$ and $\mathrm{L} = 30\mathrm{nm}$. We observe performance improvement by 300%, the room temperature mobility is calculated to be 3000 $\mathrm{cm^2/Vs}$. Such comprehensive modeling of transport enables us to predict performance for ultimately scaled device, and helps us to figure out, quantitatively, ways and means by which the degraded performance can be improved.

Bibliography

[1] D. Cheng, C. Liao, K. U. Cheng and M. Feng, "Process Development and Characteristics of Nano III-V MOSFET," *CSMANTECH*, Vol. 4, 2008.

[2] Chau, R.; Datta, S.; Majumdar, A.; , "Opportunities and challenges of III-V nanoelectronics for future high-speed, low-power logic applications," *Compound Semiconductor Integrated Circuit Symposium*, 2005. CSIC '05. IEEE , vol., no., pp. 4 pp., 30 Oct.-2 Nov. 2005 doi: 10.1109/CSICS.2005.1531740

[3] M. Passlack, R. Droopad, K. Rajagopalan, J. Abrokwah, P. Zurcher and P. Fejes, "High Mobility III-V MOSFET Technology," in *Compound Semiconductor Integrated Circuit Symposium*, 2006. CISC 2006, IEEE, 2006, pp. 39-42.

[4] Y. Sun, S. J. Koester, E. W. Kiewra, J. P. de Souza, N. Ruiz, J. J. Bucchignano, A. Callegri, K. E. Rogel and R. Germann, "Post Si-CMOS: III-V n-MOSFETs with High-k Gate Dielectrics," in *Compound Semiconductor Integrated Circuit Symposium*, May 2007.

[5] K. M. Lau, T. Chak Wah, L. Haiou and Z. Zhenyu, "AlInAs/GaInAs mHEMTs on Silicon substrates grown by MOCVD," in *Electron Devices Meeting*, 2008, IEDM 2008, IEEE International, 2008, pp. 1-4.

[6] Nguyen LD, Larson LE, Mishra UK., "Ultra-high-speed modulation doped field-effect transistors: a tutorial review," *Proc. IEEE 1992*; 80(4):494518.

[7] http://www.ioffe.ru/SVA/NSM/Semicond/index.html

[8] Brian R. Bennett, Richard Magno, J. Brad Boos, Walter Kruppa, Mario G. Ancona; "Antimonide-based compound semiconductors for electronic devices: A review," *Solid-State Electronics*, Volume 49, Issue 12, December 2005, Pages 1875-1895, ISSN 0038-1101, DOI: 10.1016/j.sse.2005.09.008.

[9] Dobrovolskis Z, Grigoras K, Krotkus A., "Measurement of the hot electron conductivity in semiconductors using ultrafast electric pulses," *Appl Phys A-Mater* 1989;48(3):2459.

[10] Chang CA, Ludeke R, Chang LL, Esaki L., "Molecular-beam epitaxy (MBE) of InGaAs and GaSbAs," *Appl Phys Lett* 1977;31(11):75961.

[11] Bennett BR, Shanabrook BV, "Molecular beam epitaxy of Sb-based semiconductors," *Thin films: heteroepitaxial systems* Singapore: World Scientific; 1999. p. 40152.

[12] Tuttle G, Kroemer H, English JH, "Electron concentrations and mobilities in AlSb/InAs/AlSb quantum wells," *J Appl Phys* 1989; 65(12):523942.

[13] Tuttle G, Kroemer H, English JH, "Effects of interface layer sequencing on the transport-properties of InAs/AlSb quantum wells evidence for antisite donors at the InAs/AlSb interface," *J Appl Phys* 1990;67(6):30327.

[14] Bolognesi CR, Kroemer H, English JH, "Well width dependence of electron-transport in molecular-beam epitaxially grown InAs/AlSb quantum-wells," *J Vac Sci Technol B* 1992;10(2):8779.

[15] A. Ali, H. Madan, R. Misra, E. Hwang, A. Agrawal, P. E. Schiffer, J. B. Boos, B. R. Bennett, I. Geppert, M. Eizenberg and S. Datta, "Advanced Composite High-k Gate Stack for Mixed Anion Arsenide-Antimonide Quantum Well Transistors", *Electron Devices Meeting (IEDM)*, Dec. 2010

[16] M. J. Yang, B. R. Bennett, M. Fatemi, P. J. Lin-Chung, W. J. Moore, and C. H. Yang, *J. Appl. Phys.* 87, 8192 (2000).

[17] S. Miya, S. Muramatsu, N. Kuze, K. Nagase, T. Iwabuchi, A. Ichii, M. Ozaki, and I. Shibasaki, *J. Electron. Mater.* 25, 415 (1996).

[18] Bart Van Zeghbroeck, Principles of Semiconductor Devices, http://www.ece.colorado.edu/ bart/book/book/title.htm, 2007.

[19] Altschul, V. Ariel; Fraenkel, A.; Finkman, E.;"Effects of band nonparabolicity on two-dimensional electron gas," *Journal of Applied Physics* , vol.71, no.9, pp.4382-4384, May 1992 doi: 10.1063/1.350775

[20] Ekenberg, U.; "Nonparabolicity effects in a quantum well: Sublevel shift, parallel mass, and Landau levels," Phys. Rev. B, vol. 40, no. 11, pp. 7714-7726, Oct. 1989

[21] Fundamentals of Carrier Transport, 2nd Edition Mark Lundstrom, Cambridge University Press ISBN-13: 9780521637244

[22] B K Ridley 1982 *J. Phys. C: Solid State Phys.* 15 5899 doi: 10.1088/0022-3719/15/28/021

[23] Walukiewicz, W.; Ruda, H. E.; Lagowski, J.; Gatos, H. C.; “Electron mobility in modulation-doped heterostructures,” *Phys. Rev. B*, vol. 30, no. 8, pp/ 4571-4582, Oct 1984

[24] Fang F F; Howard W E; *Phys. Rev. Lett.* 16 797, 1966

[25] Davies J H; The Physics of Low-Dimensional Semiconductors (Cambridge: Cambridge University Press) 1998

[26] R. Dingle; H. L. Stormer; A. C. Gossard; W. Wiegmann; *Appl. Phys. Lett.* 33 (1978) 665

[27] S. Hiyamizu; J. Saito; K. Nambu; T. Ishikawa; *Jpn. J. Appl. Phys.* 22 (1983) L609

[28] K. Lee, M. S. Shur, T. J. Drummond, H. Morkoc, “ Low field mobility of 2-d electron gas in modulation doped AlGaAs/GaAs layers,” *J. Appl. Phys.* 54 (11) Nov. 1983

[29] P. J. Price, *J. Vac. Sci. Technol.* 19, 599 (1981).

[30] Orr, J. M. S.; Gilbertson, A. M.; Fearn, M.; Croad, O. W.; Storey, C. J.; Buckle, L.; Emeny, M. T.; Buckle, P. D.; Ashley, T; “Electronic transport in modulation-doped InSb quantum well heterostructures,” *Phys. Rev. B*, vol. 77, no. 16, pp. 165334, April 2007

[31] U. Penner, H. Rcker, and I. N. Yassievich, *Semicond. Sci. Technol.* 13, 709 (1998)

[32] S. M. Goodnick, D. K. Ferry, C. W. Wilmsen, Z. Liliental, D. Fathy, and O. L. Krivanek, *Phys. Rev. B* 32, 8171 (1985)

[33] H. Sakaki, T. Noda, K. Hirakawa, M. Tanaka, and T. Matsusue, *Appl. Phys. Lett.* 51, 1934 (1987)

[34] P. J. Price, *Ann. Phys. (N.Y.)* 133, 217 (1981)

[35] A. Ali; H. S. Madan; A. P. Kirk; D. A. Zhao; D. A. Mourey; M. K. Hudait; R. M. Wallace; T. N. Jackson; B. R. Bennett; J. B. Boos; and S. Datta; “Fermi level unpinning of GaSb (100) using plasma enhanced atomic layer deposition of Al2O3,” *Appl. Phys. Lett.* 97, 143502 (2010);

[36] Tae-Woo Kim; Dae-Hyun Kim; del Alamo, J.A.; , “Logic characteristics of 40 nm thin-channel InAs HEMTs,”*Indium Phosphide & Related Materials (IPRM), 2010 International Conference on*, vol., no., pp.1-4, May 31 2010-June 4 2010

[37] Kharche, N.; Klimeck, G.; Dae-Hyun Kim; del Alamo, J.A.; Luisier, M.; , “Performance analysis of ultra-scaled InAs HEMTs,”*Electron Devices Meeting (IEDM), 2009 IEEE International*, vol., no., pp.1-4, 7-9 Dec. 2009

[38] Li Yanbo ; Zhang, Yang; Zeng, Yiping,; “Electron Mobility in modulation-doped AlSb/InAs quantum wells, *J. Appl. Phys.*109, 073703 (2011); doi:10.1063/1.3552417

[39] D. A. Mourey, D. A. Zhao, J. Sun, and T. N. Jackson; “Fast PEALD ZnO Thin-Film Transistor Circuits”, *IEEE Trans. Electron Devices* 57, 530 (2010)

[40] J. Antoszewski, D.J. Seymour, L. Faraone, J.R. Meyer, and C.A. Hoffman, “Magneto-transport characterization using quantitative mobility spectrum analysis”, *J. Electron. Mater.* 24, 1255 (1995).

[41] W.A. Beck and J.R. Anderson, “Determination of electrical transport using a novel magnetic field-dependent Hall technique ”, *J. Appl. Phys.* 62, 541 (1987).

[42] Z. Dziuba and M. Gorska, “Analysis of the electrical conduction using an iterative method”, *J. Phys. III France 2*, 110 (1992).

[43] Ali, A.; Madan, H.; Misra, R.; Agrawal, A.; Schiffer, P.; Boos, J.B.; Bennett, B.R.; Datta, S.; , “Experimental Determination of Quantum and Centroid Capacitance in ArsenideAntimonide Quantum-Well MOSFETs Incorporating Nonparabolicity Effect,” *Electron Devices, IEEE Transactions on* , vol.58, no.5, pp.1397-1403, May 2011 doi: 10.1109/TED.2011.2110652

[44] T. E. Whall, N. L. Mattey, A. D. Plews, P. J. Phillips, O. A. Mironov, R. J. Nicholas, and M. J. Kearney, “Effective mass and quantum lifetime in a Si/Si0.87Ge0.13/Si two-dimensional hole gas, *Appl. Phys. Lett.*, vol. 64, no. 3, pp. 357359, Jan. 1994.

[45] G. Moschetti, H. Zhao, P.-A Nilsson, S. Wang, A. Kalabukhov, G. Dambrine, S. Bollaert, L. Desplanque, X. Wallart and J. Grahn, “ Anisotropic transport properties in InAs/AlSb heterostructures”, *Applied Physics Letters* 97, 243510 (2010)